# Thermodynamic Modeling of Pure Elements from 0 K with Uncertainty Quantification using PyCalphad and ESPEI

Alexander M. Richter[1*], Abdulmonem Obaied[2,3], Irina Roslyakova[2,3], Boris Wilthan[4], Allison M. Beese[1], Zi-Kui Liu[1]

[1] Pennsylvania State University, Department of Materials Science and Engineering, University Park, PA 16802, USA

[2] Ruhr-Universität Bochum, ICAMS, Universitätsstrasse 150, Bochum 44801, Germany

[3]GTT-Technologies, Kaiserstraße 103, Herzogenrath 52134, Germany

[4]National Institute of Standards and Technology, Boulder, Colorado 80305, USA

*e-mail address of corresponding author: amr8004@psu.edu

**Abstract**

Thermodynamic modeling of pure elements is the foundation of the CALPHAD modeling of engineering materials. Recently, multiple physics-based models have been proposed to describe Gibbs energy of pure elements down to 0 K, extending from 298.15 K in the current CALPHAD modeling. To enable their systematic and quantitative comparison and adoption, those thermodynamic models of pure elements are implemented into the open-source software packages PyCalphad and ESPEI in the present work for evaluation of model parameters and model fitness. PyCalphad and ESPEI provide a reproducible framework for implementing and evaluating these models and offer a foundation for future high-throughput CALPHAD workflows. Particularly, Markov Chain Monte Carlo used in ESPEI allows for uncertainty quantification of model parameters and model predictions. Through the remodeling of 41 pure

elements, the present work demonstrates a systematic comparison of pure-element thermodynamic models using a consistent data and fitting workflow, thereby providing a basis for future development of multicomponent CALPHAD databases with improved pure-element descriptions

## 1 Introduction

Thermodynamic modeling based on the CALPHAD approach[1], [2], [3], [4] is the backbone of the Integrated Computational Materials Engineering (ICME)[5], [6] and the US Materials Genome Initiative[7] . While CALPHAD is typically referred to as calculation of phase diagrams pioneered by Kaufman[1], [8] , it covers both equilibrium and nonequilibrium thermodynamics[9], [10] and serves as the foundation for multiscale simulations and design of materials[5], [11], [12].

CALPHAD modeling of thermodynamics of multicomponent materials starts from the modeling of Gibbs energy of individual phases in their stable, metastable, and unstable states, first for pure elements and then moving up to binary and ternary systems. These binary and ternary models are then combined and extrapolated to describe complex alloys such as steels or nickel-base superalloys. Since these databases are built up from the pure elements, accurate thermodynamic descriptions of pure elements are critical, and any of their changes would require subsequent remodeling of all related higher-order systems[13], [14]. Their importance prompted the CALPHAD community to create a standardized database of pure element thermodynamic descriptions published in 1991[15] , serving as the foundation of the second generation of CALPHAD modeling building on its first generation[8], [16] , and commonly referred as SGTE91 database. In this database the heat capacity of an element was described by polynomials that were designed to cover the available high temperature data above 298.15 K, as used in the NIST-JANAF table[17] but also informed by additional thermochemical measurements, and the Gibbs energy differences between stable and non-stable phases of pure elements, commonly referred as lattice stability[8], [16] , were defined.  This standardized database of pure elements

has enabled the development of many valuable CALPHAD databases for thermodynamic, kinetic, and other properties of complex multicomponent materials that are widely used in academia and industry[11], [18] .

One of the major limitations of the second generation CALPHAD modeling is that it is applicable only to high temperatures and cannot be extended to low temperatures, where the heat capacity can no longer be described by simple polynomials, and physics-based models such as Debye or Einstein models are needed. Although tremendous amounts of thermodynamic data have been predicted via first-principles calculations based on density functional theory (DFT)[19], [20] , only a fraction can be directly incorporated into CALPHAD assessments because most calculations are performed for selected configurations at 0 K, while CALPHAD requires thermodynamically consistent descriptions spanning temperature, composition, and phase space. Consequently, DFT results must be combined with finite-temperature models and experimental information before database development[21]. Furthermore, since the SGTE91 database was developed more than 30 years ago, efforts have been made to improve CALPHAD modeling of pure elements, commonly referred to as the 3$^{rd}$ generation CALPHAD models. These models started with the 1995 Ringberg workshop (RW)[22] where a "universal" model was proposed for CALPHAD modeling of pure elements down to 0 K using an Einstein function and several power terms. Chen and Sundman (CS)[23] modified the RW model at high temperature and applied it to FCC, BCC, and liquid iron, and Roslyakova et al.[24] proposed a segmented regression (SR) model to replace the polynomial function in the SGTE91 model. There have been several publications on the development of 3$^{rd}$ generation CALPHAD models with extensions to binary[25], [26], [27], [28], [29], [30], [31], [32], [33], [34], [35], [36]and

ternary systems[37], [38]. In addition, three recent re-assessments employing the SR model have extended these approaches to complex high-order systems: the Mo–Nb–Ta–W refractory high-entropy alloys[39], Mo–Nb–Ta–W–Hf–Zr alloys[40], and Ti–Hf–Zr–Nb–Ta alloys[41]. These studies demonstrate that 3rd generation CALPHAD modeling is now actively used for re-assessments across a wide range of systems. However, the complete re-assessment of existing multicomponent databases would require many years of effort. This represents a major drawback for accelerating database development and for integrating more physics-based models into CALPHAD. It is noteworthy that, so far, only the SR model has been applied in re-assessments of multicomponent systems with more than four elements, underlining its importance for extending CALPHAD to high-order alloys.

Moreover, the lack of systematic revision of modeling of pure elements reflects an inherent feature of the hierarchical CALPHAD approach where the modeling of pure elements is at the foundation of binary, ternary and multicomponent systems, and any change of modeling of a pure element requires the re-modeling of all systems containing that element[13], [14] , which is practically intractable with existing data and tool infrastructure in the CALPHAD community. The key bottlenecks are the lack of robust input data repositories and the need for high-throughput CALPHAD modeling tools. Addressing these issues will allow researchers to easily evaluate and compare various models, as well as efficiently update multicomponent databases.[13], [14] . Recently, open-source tools PyCalphad[42], [43] and ESPEI[44], [45] have been developed with PyCalphad for thermodynamic models and calculations and ESPEI for efficient evaluations of model parameters using Markov Chain Monte Carlo (MCMC)

simulations and JSON files for the repository of input data. The default models of pure elements in PyCalphad and ESPEI are the SGTE91 database.

These open-source Python tools are well suited for implementing pure-element models because they provide infrastructure for reproducible and increasingly automated evaluation of model parameters. Additionally, as computational predictions from density functional theory (DFT) and machine learning (ML) methods improve, these tools may provide part of the infrastructure needed for more systematic and partially automated thermodynamic database development from pure elements toward multicomponent systems. DFT can predict Gibbs energy of configurations to enable the initial evaluations of model parameters, which are further optimized to reproduce experimental phase equilibrium data[21] . Though DFT predictions are often performed at 0 K, they can also be at finite temperature by including contributions from thermal electrons and phonons[46] . More recently, ML models have been rapidly developed with accuracy close to DFT-based calculations and much higher efficiency[47], [48], [49] . With the Helmholtz energy of both stable and metastable configurations predicted by DFT-based calculations, the multiscale entropy approach (recently termed zentropy theory) was developed to accurately obtain Gibbs energy of individual phases with emergent properties[50], [51], [52], [53] , providing a possible foundation for future workflows in which CALPHAD model parameters for individual phases can be regenerated more systematically using PyCalphad and ESPEI.

Traditional CALPHAD assessments are commonly performed using least-squares optimization tools such as PARROT[54], which often require substantial expert intervention in parameter selection, weighting of datasets, and iterative refinement of models. In contrast, ESPEI provides

an automated workflow that combines standardized thermodynamic datasets, automatic parameter generation, model selection using information criteria, and optimization within a unified framework. This reduces manual intervention and improves reproducibility, making large-scale reassessments from unary to multicomponent systems more practical. In the present work, Bayesian optimization through MCMC is used primarily for uncertainty quantification of model parameters and predictions, while the automation is enabled by the overall ESPEI workflow.

The present work implements the RW, CS, and SR models of pure elements into the PyCalphad/ESPEI ecosystem[55] and evaluates their model parameters for 41 pure elements using the available experimental heat capacity data in the literature. These experimental data are taken from the NIST Alloy Data repository[56].

## 2 Overview of Thermodynamic Models: SGTE91, RW, CS, and SR

As mentioned above, most CALPHAD software defaults to describing the temperature dependence of heat capacities with high-order polynomials fit to experimental data and then stored in the universally used SGTE91 database[15] for pure elements. The Gibbs energy function of a pure element in the nonmagnetic solid phase φ is described by the following equation:

$$^{0}G^{\varphi}(T) - H^{SER} = a + bT + cTln(T) + dT^{2} + eT^{-1} + fT^{3} + gT^{7} + hT^{-9} \qquad Eq.\ 1$$

where $H^{SER}$ is the molar enthalpy of the element at 298.15 K and $10^5$ Pa in the standard element reference (SER) state so that $H = 0$ under the SER state.

The enthalpy, entropy, and heat capacity can be derived through the following relations:

$$S = -\left(\frac{\partial G}{\partial T}\right)_P = -(b + c(1 + \ln(T)) + 2dT - eT^{-2} + 3fT^2 + 7gT^6 - 9hT^{-10}) \quad \textit{Eq. 2}$$

$$H = G + TS = G - T\left(\frac{\partial G}{\partial T}\right)_P \quad \textit{Eq. 3}$$
$$= a - cT - dT^2 + 2eT^{-1} - 2fT^3 - 6gT^7 + 10hT^{-9}$$

$$C_P = \left(\frac{\partial H}{\partial T}\right)_P = -T\left(\frac{\partial^2 G}{\partial T^2}\right)_P = T\left(\frac{\partial S}{\partial T}\right)_P \quad \textit{Eq. 4}$$
$$= -c - 2dT - 2eT^{-2} - 6fT^2 - 42gT^6 - 90hT^{-1}$$

For magnetic elements, the heat capacity due to magnetic order-disorder transition is added separately as discussed below, and contributes to enthalpy, entropy, and Gibbs energy accordingly. To extend Eq. 1 down to 0 K, the 3rd generation models for heat capacity have been developed with three parts: the Einstein or Debye model for phonon contribution, a model for additional low and high temperature effects, and a magnetic model for magnetic elements in accordance with physical contributions discussed by Grimvall[57]. The RW model is written as follows[22],

$$C_p^{RW}(T, \theta^{RW}) = C_p^{Deb/Ein}(T) + aT + bT^2 + C_p^{Magn}(T) \quad \textit{Eq. 5}$$

where the Debye and Einstein models are given by following equations

$$C_p^{Deb}(T, \theta_D) = 9R\left(\frac{T}{\theta_D}\right)^3 \int_0^{\frac{\theta_D}{T}} \frac{x^4 e^x}{(e^x - 1)^2} dx \quad \textit{Eq. 6}$$

$$C_p^{Ein}(T, \theta_E) = 3R\left(\frac{\theta_E}{T}\right)^2 \frac{e^{\frac{\theta_E}{T}}}{(e^{\frac{\theta_E}{T}} - 1)^2} \quad \textit{Eq. 7}$$

where $\theta_D$ and $\theta_E$ are the Debye and Einstein temperature, respectively. The Debye model represents a better temperature dependence at low temperatures than the Einstein model, but the integration in the Debye model makes it difficult for its implementation in the current CALPHAD modeling tools though attempts have been made to represent it by a combination of two Einstein functions in several systems[25], [26], [27], [39], [40], [41].

The magnetic contribution to heat capacity has been described by the Inden-Hillert-Jarl model[58], which was subsequently revised by Chen and Sundman[23] and further refined by Xiong et al.[59]. Although the model by Xiong et al. was primarily developed for binary and multicomponent systems, its formulation is applicable to pure elements and is used as such in the present work. The present work adopts the formulation by Xiong et al. as follows:

$$C_p^{Magn} = RT * g(\tau) * \ln(\beta^* + 1) \qquad \textit{Eq. 8}$$

$$g(\tau) = \begin{cases} \frac{0.63570895}{A}\left(\frac{1}{p} - 1\right)\left(2\tau^3 + 2\frac{\tau^9}{3} + 2\frac{\tau^{15}}{5} 2\frac{\tau^{21}}{7}\right), \tau \le 1 \\ \frac{1}{A}\left(2\tau^{-7} + 2\frac{\tau^{-21}}{3} + 2\frac{\tau^{-35}}{5} + 2\frac{\tau^{-49}}{7}\right), \tau \ge 1 \end{cases} \qquad \textit{Eq. 9}$$

$$A = 0.33471979 + 0.49649686\left(\frac{1}{p} - 1\right) \qquad \textit{Eq. 10}$$

where $\tau$ equals $T/T^*$, with $T^*$ being the magnetic Curie or Néel temperature, $\beta^*$ is the effective magnetic momentum per atom, and $p$ is the structure factor defined as the ratio of the magnetic enthalpy in the paramagnetic state to the total magnetic enthalpy.

In the CS model developed for iron[23], the $T^2$ term in the RW model with Einstein model was replaced by $T^4$ as they found better agreement with high-temperature heat capacity data as follows:

$$C_p^{CS} = C_p^{Ein} + aT + bT^4 + C_p^{Magn} \qquad \textit{Eq. 11}$$

In the SR model[24] segments are smoothly jointed in a temperature range by quadratic bends, as follows:

$$C_p^{SR} = C_p^{Ein} + C_p^{BCM} + C_p^{Magn} \qquad \textit{Eq. 12}$$

$$C_p^{BCM} = \beta_1 T + \beta_2 * q(\tau, \gamma) \qquad \textit{Eq. 13}$$

$$q(\tau,\gamma) = f(x) = \begin{cases} 0, & T < \tau - \gamma \\ \dfrac{(T-\tau+\gamma)^2}{4\gamma}, & \tau - \gamma \le T \le \tau + \gamma \\ T - \gamma, & T > \tau + \gamma \end{cases} \qquad \textit{Eq. 14}$$

where the temperature range is defined by $\tau$-$\gamma$ and $\tau$+$\gamma$ with $\beta_1$ and $\beta_1 + \beta_2$ being the slopes at $\tau$-$\gamma$ and $\tau$+$\gamma$, respectively. It is noted that in the SR model, there are four fitting parameters in addition to those in $C_p^{Deb/Ein}$ and $C_p^{Magn}$, i.e., $\tau$, $\gamma$, $\beta_1$, and $\beta_2$, while in the RW and CS models, there are only two additional parameters, i.e., $a$ and $b$.

With the heat capacity model parameters evaluated, entropy, enthalpy, and Gibbs energy can be obtained by integrations of Eqs. 15-17 as follows:

$$S = \int_0^T \frac{C_p}{T} dT \qquad \textit{Eq. 15}$$

$$H = \int_0^T C_p dT - H_0 \qquad \textit{Eq. 16}$$

$$G = H - TS \qquad Eq.\ 17$$

where $H_0$ represents the enthalpy at 298.15 K so that $H$=0 at the SER state used in CALPHAD modeling. For consistency across model forms, the RW, CS, and SR heat capacity expressions were evaluated using a single Einstein vibrational contribution and the same experimental datasets and fitting workflow. This allows differences among the calculated thermodynamic properties to be attributed primarily to the model formulations rather than to differences in data selection or fitting procedure. The implementation also provides a framework for incorporating and comparing additional pure element heat capacity models in future work.

The goal of the present work is not to propose new thermodynamic models, but to systematically implement, compare, and quantify uncertainty for existing pure element models within a unified PyCalphad and ESPEI framework. By applying identical data, fitting procedures, and statistical metrics to the RW, CS, and SR models across 41 elements, this work enables transparent model comparison and provides a scalable foundation for future CALPHAD database updating workflows and integration of additional physics-based models.

## 3 Computational Workflow and Statistical Framework

### 3.1 Brief Overview of PyCalphad and ESPEI

As previously mentioned, revising a pure element within a multicomponent system requires extensive re-modeling of many systems, as illustrated in Figure 1. Automating this reassessment process would significantly facilitate the development of new models. PyCalphad and ESPEI provide a foundation for this automation.

*Figure 1 Circled systems to be remodeled in a hypothetical 6 element database of A-B-C-D-E-F, if the thermodynamic description of pure Element "C" is modified, reproduced from Ref. [13].*

PyCalphad is an open-source Python library for creating thermodynamic models, calculating thermodynamic properties and phase diagrams, and investigating driving forces and phase equilibria[42] . It plays a significant role in computational thermodynamics by providing a flexible and powerful framework for modeling complex systems. PyCalphad is designed with models represented symbolically by leveraging symbolic mathematics to define and manipulate thermodynamic models. This greatly facilitates the inclusion of additional custom models.

ESPEI is a Python tool built on PyCalphad for evaluating model parameters and uncertainty of CALPHAD models[44]. ESPEI operates in two stages: estimation and optimization of model parameter values. During the estimation stage, ESPEI employs a linear fitting strategy to parameterize Gibbs energy functions of single phases based on their thermochemical data, which are derivatives of Gibbs energy. In the optimization stage, ESPEI refines model parameters through Bayesian parameter evaluation with MCMC simulations. ESPEI can simultaneously utilize experimental thermochemical, computational thermochemical, activity, and phase equilibrium data during optimization. In the present work, experimental heat capacity data constitute the primary source of information used to evaluate the pure-element model parameters.

### 3.2 Bayesian Parameter Optimization and Uncertainty Quantification

To perform Bayesian optimization, ESPEI uses an affine-invariant ensemble MCMC sampler to explore the parameter space. Rather than operating as independent chains, the walkers form an ensemble and generate new proposals based on the positions of other walkers in the ensemble. This collective sampling strategy improves exploration of complex and correlated parameter spaces and reduces the likelihood of becoming trapped in local minima. As sampling proceeds, the ensemble generates samples from the posterior distribution of the model parameters conditioned on the prior assumptions and experimental data. The resulting posterior distributions provide both optimal parameter estimates and a basis for uncertainty quantification (UQ) of thermodynamic properties.

Experimental heat capacity uncertainties were incorporated directly into the likelihood function used for MCMC sampling. The likelihood assumes normally distributed residuals between experimental and calculated heat capacities, with each residual weighted by its corresponding uncertainty. When point-specific experimental uncertainties were available, those values were used directly. When uncertainty metadata were unavailable, as was the case for many literature values collected through the NIST database, a default absolute uncertainty of 0.2 J mol−1 K−1 was assigned. This value was selected as a representative calorimetric heat-capacity uncertainty and was used only when dataset-specific uncertainty information was unavailable and is consistent with uncertainties used in prior ESPEI publications [44]. Because the same uncertainty model was applied consistently to all competing models for a given element, the resulting AICc-based model rankings remain internally consistent across the RW, CS, and SR models.

Sampling behavior was assessed using both visual and quantitative diagnostics. Trace plots were inspected to confirm stabilization of the sampled parameters and log-likelihood after burn-in and to verify the absence of systematic drift in the retained samples. Convergence can be further assessed by means of several criteria common to MCMC simulations, as detailed by Gelman et al.[60]. The uncertainty propagation, particularly to higher order systems, was investigated by Paulson et al. [61], who further considered two weighting methods to quantify uncertainty of experimental data sets used in the *Cp*-data of Al and Hf with the SR model[62].

### 3.3 Model comparison Using AICc

Model comparison was performed after MCMC refinement using the corrected Akaike information criterion (AICc)[63]. In the present work, AICc was used to compare the RW, CS, and SR models for each element using the same heat-capacity dataset and fitting workflow.

The Akaike information criterion is defined as:

$$AIC = -2\ln L + 2k, \qquad \textit{Eq. 18}$$

where L is the likelihood and k the number of adjustable parameters. For normally distributed residuals, the log-likelihood under maximum likelihood estimation can be written in terms of the residual sum of squares, RSS, as:

$$\ln L_{MLE} = -\frac{n}{2}\ln\frac{RSS}{n} + C. \qquad \textit{Eq. 19}$$

where n is the number of data points and and C is a constant[64]. Since C is constant for all models compared using the same dataset, it can be ignored when just comparing one dataset. As such AIC becomes:

$$AIC = n\ln\frac{RSS}{n} + 2k \qquad \textit{Eq. 20}$$

The AICc adds an additional penalty for models with larger numbers of parameters, especially when the number of data points is limited [63]:

$$AICc = AIC + \frac{2k^2 + 2k}{n - k - 1} = n \ln \frac{RSS}{n} + 2k + \frac{2k^2 + 2k}{n - k - 1} = n \ln \frac{RSS}{n} + \frac{2kn}{n - k - 1} \qquad \textit{Eq. 21}$$

Lower AICc values indicate better statistical support after accounting for model complexity. Because AICc depends on the likelihood, the absolute AICc values depend on the uncertainty model used in the likelihood function. However, for each element, the same heat-capacity data and uncertainty assumptions were applied consistently to the RW, CS, and SR models. Therefore, the AICc rankings provide an internally consistent comparison among the competing model forms for each dataset.

## 4 Modeling Procedure

The SGTE91 database contains 81 elements. 41 pure elements were considered in the present work with data collected so far, and extension to all elements in the periodic table is being considered. Of the 41 elements, the majority were directly collected from the alloy database maintained by the Thermodynamics Research Center (TRC) at the National Institute of Standards and Technology (NIST)[56]. It is curated by experts with a focus on the elements, binary and ternary alloys from open literature spanning from the early 1900s to recent publications, including properties such as density, specific heat, viscosity, enthalpy, phase transition temperatures, and more. Regardless of whether the original data are presented in tables, equations, or graphs, they are digitized and accompanied by metadata, provenance details, and uncertainty assessments. The database is accessible via a user-friendly web application[56] that offers both a graphical periodic table

interface for simple searches and advanced options for complex queries with additional data analysis tools. Programmatic access is also available through an API, enabling efficient use of the structured data in electronic formats.

In the present work, pure element heat capacity data was systematically collected from the NIST database and converted to JSON format for maximum compatibility with ESPEI. Additionally, data for Al[24], Cr[65], and Fe[24] collected in previous publications and for Ge, Se, and Si curated in the present work were also utilized due to comprehensive analysis from various sources and compared with those from NIST database. All data used in the work is available in the GitHub repository[66] associated with this work. Heat capacity data in JSON format is the only mandatory input for fitting, as all models as well as the functionality are already implemented.

Models were manually added to PyCalphad, using symbolic representation of Eq. 5, Eq. 11, and Eq. 12 and their corresponding Gibbs energy functions. Magnetic contributions, where applicable, are incorporated using parameters such as Curie temperature, $\beta^*$, and p. These magnetic parameters are not supplied by standard PyCalphad. Instead, they were provided through an auxiliary parameter table developed in this work and automatically loaded by the workflow during model construction. The tabulated values can be adjusted when improved magnetic data or element-specific assessments are available.

Bayesian parameter estimation was carried out using ensemble Markov Chain Monte Carlo (MCMC) sampling applied to the symbolic model functions. An ensemble of walkers was used to explore the parameter space collectively, rather than as independent chains. Bounded uniform

priors were used during MCMC sampling. Within the specified bounds, all parameter values were assigned equal prior probability, while parameter sets outside the admissible ranges were assigned zero posterior probability. These priors were chosen to be broad enough to allow exploration of the parameter space while preventing nonphysical or numerically unstable heat-capacity behavior. The Einstein temperature was constrained to remain positive because negative Einstein temperatures are nonphysical. For the RW and CS models, the priors were $\theta E \sim$ Uniform(0, 700 K), $a \sim$ Uniform(0, 0.1), and $b \sim$ Uniform(0, 0.1). For the SR model, the priors were $\theta E \sim$ Uniform(0, 700 K), $\beta 1 \sim$ Uniform(0, 0.1), $\beta 2 \sim$ Uniform(0, 0.1), $\tau \sim$ Uniform($-20000$, 20000), and $\gamma \sim$ Uniform($-20000$, 20000).

In this work, an ensemble of 48 walkers was run for up to 10,000 MCMC steps, with an initial burn-in region discarded prior to posterior analysis. Sampling behavior was evaluated by diagnostic inspection of trace plots, stabilization of the log-likelihood, and absence of systematic drift after burn-in. The retained posterior samples were then used to quantify parameter uncertainty. The best-fit parameter set was selected from the retained MCMC samples as the parameter vector with the highest posterior probability. Because bounded uniform priors were used, this is equivalent to selecting the retained sample with the highest likelihood within the allowed parameter bounds. Marginal posterior medians and credible intervals were used only to summarize uncertainty in individual parameters and were not used to construct the best-fit parameter vector.

Figure 2 shows the MCMC traces and corresponding corner plot for Cr using the CS model. The diagonal panels of the corner plot show the marginal posterior distributions of individual parameters, while the off-diagonal panels show two-dimensional posterior densities illustrating correlations between parameter pairs. These correlations demonstrate why the best-fit parameter

set must be selected from the joint posterior distribution rather than constructed from independent marginal medians. In this example, the parameters $a$ and $b$ exhibit a moderate negative correlation, while $\theta_E$ shows weaker correlation with the other parameters. The posterior distribution of b remains close to zero, indicating that the higher order term contributes only weakly within the fitted temperature range for this Cr example.

*Figure 2 Convergence of MCMC chains for parameters $\theta_E$, a, and b (top) and the corresponding corner plot (bottom) showing posterior distributions and parameter correlations for Cr using the CS model.*

The optimized models can also be validated by comparing calculated thermodynamic properties, such as Gibbs energy, enthalpy, and entropy, with established databases. Model performance is further evaluated using AICc, computed from the log-likelihood of the data given the fitted parameters. Results, including best-fit parameters and performance metrics, are stored in structured output files for subsequent analysis and comparison across elements.

This workflow provides a robust framework for integrating curated experimental data with advanced CALPHAD modeling techniques, enabling systematic parameter optimization and uncertainty quantification for pure elements.

## 5 Modeling Results and Discussions

Among the 41 elements studied, detailed results for four representative elements (Al, Cr, Zn, Fe) are presented in the main text, while results for the remaining elements are provided in the supplementary materials. They are selected to showcase face centered cubic (FCC, Al), body centered cubic and magnetic (BCC, Cr and Fe), and hexagonal close packed (HCP, Zn) elements, respectively. Elements were included based on the availability of suitable experimental heat capacity data and whether the present single-phase fitting workflow could be applied without explicitly treating solid-solid phase transformations. The present work focuses on fitting one experimentally available stable solid phase for each element using the available heat capacity data. In this context, the modeled phase should be understood as the selected stable or reference solid phase used in the present one-phase fitting workflow, rather than as a complete reassessment of all competing crystallographic configurations or solid-solid phase transformations. The modeling of phases stable at high temperatures and liquid will be modeled in our future work. Einstein temperatures ($\theta_E$) of the 41 elements from the three models are listed in Table 1. Their AICc are listed in Table 2. It should be emphasized that the fitted Einstein temperature obtained in the present work is an effective parameter optimized to reproduce experimental heat capacity data over a finite temperature range, rather than a direct physical Debye temperature derived from elastic constants or phonon dispersion measurements. As a result, deviations from values estimated from Debye temperatures reported in the literature are expected, particularly for elements with limited low temperature data, strong elastic anisotropy, or significant anharmonic effects. Consequently, agreement with tabulated reference values should not be interpreted as a measure of fitting quality, and discrepancies do not indicate deficiencies in the modeling procedure. All

input data and scripts are provided in the supplementary materials and are also available in Jupyter notebooks within the GitHub documentation[66].

*Table 1 Einstein parameter θE in kelvin evaluated for three models and compared to θE recalculated from $\theta E \cong 0.77\theta D$ [57] collected from Kittel [67]*

### 5.1 FCC Elements

The selected low-temperature stable or reference solid phase is FCC for the following 11 elements modeled: Ag, Al, Au, Ca, Cu, Ir, Ni, Pb, Pd, Pt, Rh. Al was used as an example case for FCC, chosen for its common use and representative behavior of FCC elements. The only major outlier in FCC is the segmented regression model for pure Ca. Although heavy manual alterations could lead to a successful fit, the success of two other models indicated that the data was of sufficient quality for modeling, so further adjustments were not pursued.

The low accuracy at very low temperatures, where all models underestimate the heat capacity compared to experimental data, stems from the Einstein model's assumption that all atoms vibrate at a single frequency, which oversimplifies the true phonon spectrum of a solid. As Kittel describes, this leads to a failure to reproduce the characteristic $T^3$ dependence of heat capacity at low temperatures[67] . While the Debye model addresses this by incorporating a full distribution of vibrational modes, its implementation is more complex due to the required numerical integration.

Overall, the models show good agreement with experimental data and the SGTE91 Gibbs energies as seen in Figure 3, where all models shown are indistinguishable from each other for heat capacity, enthalpy, entropy, and Gibbs energy. The experimental data is shown in the heat capacity plot, where darker points indicate overlapping values. The spread in the data highlights experimental variability and underscores the importance of incorporating uncertainty in model predictions. It can be noted that as the temperature increases the Gibbs energy diverges from the SGTE91 Gibbs model. The underestimation of heat capacity at low temperatures is also evident, particularly below 100 K, where the models noticeably underpredict experimental values as discussed above.

*Figure 3 Thermodynamic properties of Al with three models: (a) Heat capacity with experimental data superimposed; (b) ΔEnthalpy, (c), Entropy, (d) Gibbs energy, and (e) Gibbs energy difference with respect to the SGTE91 database.*

### 5.2 BCC Elements

The selected low-temperature stable or reference solid phase is BCC for 11 elements modeled in the present work: Cr, Cs, Fe, K, Mo, Na, Nb, Rb, Ta, V and W. Cr was chosen as an example for BCC with heat capacity, enthalpy, entropy and Gibbs energy shown in Figure 4. Figure 4 highlights an important trend that occurs frequently in the heat capacity of the CS model. As shown in Figure 4a, the heat capacity starts to increase rapidly around the melting point due to the $T^4$ term. This trend is also present in the RW and SR models, but to a lesser degree. The modeling of heat capacity of solid phases above melting temperature is actively researched in the community[65], [68] and is being dealt with in our ongoing work. In addition, the

antiferromagnetic behavior of Cr, which is known to influence thermodynamic properties at low temperatures, is not considered in the present assessment.

The three models differ noticeably in their descriptions, with a higher variation than what is seen in FCC Al. This increased variance is primarily due to the scatter in high-temperature experimental data, which prevents a clear trend and complicates the fitting process. Since the resulting fits of the three models are no longer nearly identical and more significant differences arise among them, a quantitative model comparison is useful for determining which model best suits the element.

*Figure 4 Thermodynamic properties of Cr with three models: (a) Heat capacity with experimental data superimposed; (b) ΔEnthalpy, (c) Entropy, (d) Gibbs energy, and (e) Gibbs energy difference with respect to the SGTE91 database*

### 5.3 HCP Elements

The selected low-temperature stable or reference solid phase is HCP for 9 elements modeled in the present work: Be, Cd, Hf, Mg, Re, Sc, Tl, Y, and Zn. Zn was selected to demonstrate as shown in Figure 5. All models behave similarly for Zn at lower temperatures but begin to diverge as temperature increases. This behavior is expected because differences in model formulations become more influential at elevated temperatures. Since Zn has a relatively low melting point and correspondingly low Debye temperature, the vibrational contribution remains significant across a broader portion of the temperature range compared to elements with higher Debye temperatures. This may explain a notable feature in Figure 5, where after the underprediction by the Einstein model between 5 and 10 K, Zn exhibits a visually apparent overprediction between 50 and 100 K.

This occurs because the Einstein model's contribution increasing rapidly whereas the experimental values rise more gradually with temperature.

Overall, model performance for HCP elements is more varied compared to the high consistency seen in FCC and BCC elements. This variability is largely due to their limited and often incomplete experimental heat capacity data. For example, experimental data for Be was only available for up to 300 K, so fitting was restricted to that range. This introduces high uncertainty in the model's predictions at higher temperatures. Despite these challenges, the models can still perform well for HCP elements when the available data, even if limited, is internally consistent and spans a temperature range that is physically meaningful, capturing the dominant vibrational behavior at low temperatures and extending sufficiently toward higher temperatures to constrain the model parameters effectively.

*Figure 5 Thermodynamic properties of Zn with three models: (a) Heat capacity with experimental data superimposed; (b) ΔEnthalpy, (c) Entropy, (d) Gibbs energy, and (e) Gibbs energy difference with respect to the SGTE91 database*

### 5.4 Magnetic Elements

Four elements were modeled with magnetic contributions by Eq. 8, Eq. 9, and Eq. 10: HCP-Co, BCC-Fe, α-Mn, FCC-Ni. The results for Fe can be seen in Figure 6. The magnetic peak is clearly represented in the heat capacity, which is carried through the S and H curves. It reflects the loss of magnetic ordering near the Curie temperature. In the present implementation, the magnetic contribution is not fitted during MCMC sampling but is instead calculated from the supplied

magnetic parameters. Therefore, the same magnetic contribution is added to each of the three heat-capacity models for a given element. As a result, the uncertainty quantified in the present work reflects uncertainty in the fitted nonmagnetic heat-capacity parameters, while uncertainty in the supplied magnetic parameters is not yet propagated.

Since BCC-Fe transforms to FCC-Fe at 1185 K, and the current tool does not automatically handle solid-solid phase transformation, only experimental heat capacity data below this temperature is included in the diagram, showing good agreement between calculated and experimental data. The calculated $C_P$, H, S, and G agree with those from the SGTE91 description.

While the magnetic systems exhibited similar overall behavior, the differences between our results and SGTE values were consistently larger for magnetic materials than for nonmagnetic materials. However, despite exhibiting the greatest difference from SGTE, the magnetic contribution based on Xiong et al.[59] reproduces the experimental behavior across all four elements in all three models.

*Figure 6 Thermodynamic properties of Fe with three models: (a) Heat capacity with experimental data superimposed; (b) ΔEnthalpy, (c) Entropy, (d) Gibbs energy, and (e) Gibbs energy difference with respect to the SGTE91 database*

### 5.5 Other Elements

Eight additional elements were modeled in the present work, including As, Bi, Ge, Hg, La, Sb, Sn, Si, for which the selected stable or reference solid phases are not FCC, BCC, or HCP. They perform similarly to other systems with the only outlier being difficulties with the segmented regression model for Si. Like with all other elements, all data and fittings can be found in the GitHub repository

### 5.6 Model Uncertainty and Posterior Prediction

The resulting AICc values for each element and model are summarized in Table 2. As described above, lower AICc values indicate stronger statistical support after accounting for model complexity, and the model with the lowest AICc value for each element is printed in bold.

*Table* 2 AICc values of RW, CS and SR models

Among 41 elements studied, the SR, CS, and RW models were found to be the best fit for 17, 14, and 10 elements, respectively. However, the differences between models are small, and other criteria that are being implemented to expand the comparison between models[69] will be used to further rank the models. In addition to model selection, UQ of the parameters was performed using MCMC simulations. As described in the procedure section, uncertainty arises both from the input data and from the spread of parameter values across converged chains. The resulting posterior distributions provide insight into the confidence of each parameter estimate. While not shown in detail here, these distributions can be used to propagate uncertainty into

thermodynamic predictions[61], offering a more robust basis for model comparison and application.

The Gibbs energy differences relative to SGTE should be interpreted with care. Although differences in the order of 1 kJ/mol can be important for phase stability, the present work fits one selected solid phase using heat capacity data and does not perform a full multiphase critical assessment. Consequently, the SGTE differences shown in Figures 3e-6e should be viewed as indicators of deviations between model forms rather than as direct measures of phase-stability errors. Propagating the MCMC parameter uncertainty to Gibbs energy is an important next step for assessing the statistical significance of these differences, particularly in cases where the deviations exceed typical phase-stability energy scales.

The propagated uncertainty in model predictions is illustrated in Figure 7, for the heat capacity of BCC Cr fitted with the SR model. For each retained posterior sample, the heat capacity was calculated to generate a posterior predictive distribution. The black line represents the heat capacity prediction corresponding to the highest likelihood parameter set for Cr. The shaded region indicates the range of predictions generated from the retained posterior samples and illustrates the propagation of parameter uncertainty to the predicted heat capacity. As shown, uncertainty increases with temperature, particularly beyond the melting point due to the lack of experimental Cp data for solid Cr above its melting temperature.

Figure 7 Heat capacity of BCC Cr from the CS model with uncertainty propagated from retained MCMC samples. The black line shows the highest likelihood parameter, and the gray region shows the range of predictions generated from the posterior samples.

## 6 Conclusion

The three existing heat capacity models of pure elements from 0 K to high temperature are implemented to the open-source PyCalphad and ESPEI frameworks, enabling systematic comparison of their performance using the same set of data and procedures. This new capability is tested for 41 pure elements in the present work, demonstrating its efficiency for CALPHAD modeling with uncertainty quantification. New models could be easily added and compared with existing models along with any new theoretical and experimental data. The present capability is being extended to include models for solid phases above the melting temperature and liquid phases above and below the melting temperature, with the goal of providing infrastructure for increasingly automated CALPHAD workflows.

## 7 Code and Data Availability

Instructions for the PyCalphad and ESPEI downloads as well as a Jupyter notebook for application of codes can be found at https://github.com/amr8004/PureElementPRL. All data shown in the current work is also available in the PureElementPRL github repository[66]. The experimental data is available from NIST Metals Alloy User Interface at https://trc.nist.gov/metals_data/. If GitHub codespaces are available, https://github.com/amr8004/3rdGenerationToolCodespace can be run and will enable use of the

tool through GitHub's UI on web.

## 8 CRediT authorship contribution statement

**Alexander M. Richter**: Conceptualization, Methodology, Software, Validation, Visualization, Writing – Original Draft. **Abdulmonem Obaied**: Methodology, Data Curation, Writing - Review & Editing. **Irina Roslyakova**: Conceptualization, Methodology, Data Curation, Writing - Review & Editing. **Boris Wilthan**: Data Curation, Writing - Review & Editing.

. **Allison M**. **Beese**: Funding acquisition, Resources, Supervision, Writing - Review & Editing. **Zi-Kui Liu**: Funding acquisition, Resources, Supervision, Writing - Review & Editing.

## 9 Declaration of Competing Interest

The authors declare that they have no known competing financial interests or personal relationships that could have appeared to influence the work reported in this paper.

## 10 Acknowledgements

The authors thank Brandon Bocklund and Richard Otis for developing the open-source tools and for their support in extending and building upon their work. This work was funded by grant contract No. N00014-21-1-2608 from the Office of Naval Research. Irina Roslyakova acknowledges the financial support from the Collaborative Research Center Superalloys Single Crystal (SFB TR-103 project T2) of the German Research Foundation (DFG). We honor the memory of our co-author, Abdulmonem Obaied, who passed away recently.

## 11 References


[1] L. Kaufman and H. Bernstein, *Computer calculation of phase diagrams with special reference to refractory metals*. 1970.

[2] N. Saunders and a. P. Miodownik, "CALPHAD--A Comprehensive Guide," vol. 1, pp. 1–479, 1998, Accessed: Sep. 12, 2025. [Online]. Available: http://linkinghub.elsevier.com/retrieve/pii/S0735821098800095

[3] H. L. Lukas, S. G. Fries, and B. Sundman, *Computational thermodynamics: The Calphad method*, vol. 9780521868. Cambridge University Press, 2007. doi: 10.1017/CBO9780511804137.

[4] Z.-K. Liu and Y. Wang, "Computational Thermodynamics of Materials," *Comput. Thermodyn. Mater.*, Apr. 2016, doi: 10.1017/CBO9781139018265.

[5] G. B. Olson, "Computational Design of Hierarchically Structured Materials," *Science (80-. ).*, vol. 277, no. 5330, pp. 1237–1242, Aug. 1997, doi: 10.1126/science.277.5330.1237.

[6] N. R. C. Committee on Integrated Computational Materials Engineering, *Integrated computational materials engineering: a transformational discipline for improved competitiveness and national security*. National Academies Press Washington, DC, 2008.

[7] C. Kalil Tom And Wadia, "Materials Genome Initiative for Global Competitiveness," *Genome*, no. June, pp. 1–18, 2011, [Online]. Available: http://www.whitehouse.gov/sites/default/files/microsites/ostp/materials_genome_initiative-final.pdf

[8] L. Kaufman, "The lattice stability of metals—I. Titanium and zirconium," *Acta Metall.*, vol. 7, no. 8, pp. 575–587, Aug. 1959, doi: 10.1016/0001-6160(59)90195-6.

[9] Z. K. Liu, "Thermodynamics and its prediction and CALPHAD modeling: Review, state

of the art, and perspectives," in *Zentropy: Theory and Fundamentals*, New York: Jenny Stanford Publishing, 2024, pp. 273–348. doi: 10.1201/9781032692401-5.

[10] Z.-K. Liu, "On Gibbs Equilibrium and Hillert Nonequilibrium Thermodynamics," *J. Phase Equilibria Diffus.*, vol. 45, no. 6, pp. 965–985, Dec. 2024, doi: 10.1007/s11669-024-01157-0.

[11] G. B. Olson and Z. K. Liu, "Genomic materials design: Calculation of phase dynamics," in *Zentropy: Tools, Modelling, and Applications*, Jenny Stanford Publishing, 2024, pp. 275–307. doi: 10.1201/9781003514466-14.

[12] K. Hack, *The SGTE Casebook: Thermodynamics at Work*. Woodhead Pub. ; CRC Press, 2024. doi: 10.1201/9781003575917.

[13] C. E. Campbell, U. R. Kattner, and Z.-K. Liu, "The development of phase-based property data using the CALPHAD method and infrastructure needs," *Integr. Mater. Manuf. Innov.*, vol. 3, no. 1, pp. 158–180, Dec. 2014, doi: 10.1186/2193-9772-3-12.

[14] C. E. Campbell, U. R. Kattner, and Z. K. Liu, "File and data repositories for Next Generation CALPHAD," *Scr. Mater.*, vol. 70, no. 1, pp. 7–11, Jan. 2014, doi: 10.1016/j.scriptamat.2013.06.013.

[15] A. T. Dinsdale, "SGTE data for pure elements," *Calphad*, vol. 15, no. 4, pp. 317–425, 1991, doi: 10.1016/0364-5916(91)90030-N.

[16] L. Kaufman, "The stability of metallic phases," *Prog. Mater. Sci.*, vol. 14, no. 2, pp. 57–96, Jan. 1969, doi: 10.1016/0079-6425(69)90001-2.

[17] "NIST-JANAF Thermochemical Tables." Accessed: Sep. 12, 2025. [Online]. Available: https://janaf.nist.gov/

[18] P. J. Spencer, "The origins, growth and current industrial impact of Calphad," *Calphad*,

vol. 79, p. 102489, Dec. 2022, doi: 10.1016/J.CALPHAD.2022.102489.

[19] I. E. Gaa, P. Hohenbergt Ecole, X. Superzeure, I'aris, F. And, and W. Konnt, "Inhomogeneous Electron Gas," *Phys. Rev.*, vol. 136, no. 3B, p. B864, Nov. 1964, doi: 10.1103/PhysRev.136.B864.

[20] W. Kohn and L. J. Sham, "Self-Consistent Equations Including Exchange and Correlation Effects," *Phys. Rev.*, vol. 140, no. 4A, p. A1133, Nov. 1965, doi: 10.1103/PhysRev.140.A1133.

[21] Z.-K. Liu, "First-principles calculations and CALPHAD modeling of thermodynamics," *J. phase equilibria Diffus.*, vol. 30, no. 5, pp. 517–534, 2009.

[22] "Workshop on thermodynamic models and data for pure elements and other endmembers of solutions: Schloβ Ringberg, Feb. 26 to March 3, 1995," *Calphad*, vol. 19, no. 4, pp. 437–447, 1995, doi: https://doi.org/10.1016/0364-5916(96)00002-8.

[23] Q. Chen and B. Sundman, "Modeling of thermodynamic properties for Bcc, Fcc, liquid, and amorphous iron," *J. Phase Equilibria*, vol. 22, no. 6, pp. 631–644, 2001, doi: 10.1007/s11669-001-0027-9.

[24] I. Roslyakova, B. Sundman, H. Dette, L. Zhang, and I. Steinbach, "Modeling of Gibbs energies of pure elements down to 0 K using segmented regression," *Calphad*, vol. 55, pp. 165–180, Dec. 2016, doi: 10.1016/j.calphad.2016.09.001.

[25] Y. Jiang, S. Zomorodpoosh, I. Roslyakova, and L. Zhang, "Thermodynamic re-assessment of binary Cr-Nb system down to 0 K," *Calphad*, vol. 62, pp. 109–118, 2018, doi: https://doi.org/10.1016/j.calphad.2018.06.001.

[26] Y. Jiang, S. Zomorodpoosh, I. Roslyakova, and L. Zhang, "Thermodynamic re-assessment of binary Cr-Nb system down to 0 K," *Calphad*, vol. 62, pp. 109–118, Sep. 2018, doi:

10.1016/j.calphad.2018.06.001.

[27] E. Zhang, X. Xu, Y. Chen, and Y. Tang, “Third-Generation Thermodynamic Descriptions for Ta-Cr and Ta-V Binary Systems,” *Materials (Basel).*, vol. 15, no. 6, 2022, doi: 10.3390/ma15062074.

[28] S. Bigdeli and M. Selleby, “A thermodynamic assessment of the binary Fe-Mn system for the third generation of Calphad databases,” *Calphad*, vol. 64, pp. 185–195, Mar. 2019, doi: 10.1016/J.CALPHAD.2018.11.011.

[29] A. Walnsch, A. Leineweber, and M. J. Kriegel, “A third generation CalPhaD assessment of the Fe–Mn–Ti system part I: The binary subsystems Fe–Mn, Fe–Ti and Mn–Ti,” *Calphad*, vol. 81, p. 102555, Jun. 2023, doi: 10.1016/j.calphad.2023.102555.

[30] G. Deffrennes *et al.*, “Thermodynamic modelling of the Ca–O system including 3rd generation description of CaO and CaO2,” *Calphad*, vol. 69, p. 101764, Jun. 2020, doi: 10.1016/j.calphad.2020.101764.

[31] L. Hao, S. Bigdeli, and W. Xiong, “From Zero Kelvin Upwards: Thermodynamic Modeling of the Mn-Ni System with Third Generation Calphad Models,” *J. Phase Equilibria Diffus.*, vol. 45, no. 6, pp. 1182–1193, Dec. 2024, doi: 10.1007/s11669-024-01165-0.

[32] Z. He, B. Kaplan, H. Mao, and M. Selleby, “The third generation Calphad description of Al–C including revisions of pure Al and C,” *Calphad*, vol. 72, p. 102250, Mar. 2021, doi: 10.1016/j.calphad.2021.102250.

[33] L. Hao, C. Shen, N. M. Fortunato, H. Zhang, and W. Xiong, “Third generation Calphad: Thermodynamic assessment of the Ni-Ga system with physics-based models,” *Calphad*, vol. 88, p. 102797, Mar. 2025, doi: 10.1016/j.calphad.2024.102797.

[34] Z. He and M. Selleby, “A third generation Calphad description of W–C including a revision of liquid C,” *Calphad*, vol. 78, p. 102449, Sep. 2022, doi: 10.1016/j.calphad.2022.102449.

[35] A. V. Khvan, A. T. Dinsdale, and Q. Chen, “Use of third generation data for the elements to model the thermodynamics of binary alloy systems: Part 2 – The critical assessment of data for the Pb-Sn system,” *Calphad*, vol. 76, p. 102396, Mar. 2022, doi: 10.1016/j.calphad.2022.102396.

[36] A. Dinsdale, O. Zobac, A. Kroupa, and A. Khvan, “Use of third generation data for the elements to model the thermodynamics of binary alloy systems: Part 1 – The critical assessment of data for the Al-Zn system,” *Calphad*, vol. 68, p. 101723, Mar. 2020, doi: 10.1016/j.calphad.2019.101723.

[37] A. Walnsch, A. Leineweber, and M. J. Kriegel, “A third generation CalPhaD assessment of the Fe–Mn–Ti system Part II: The ternary system Fe–Mn–Ti,” *Calphad*, vol. 81, p. 102553, Jun. 2023, doi: 10.1016/J.CALPHAD.2023.102553.

[38] O. Zobac, A. Kroupa, and A. Dinsdale, “Use of third generation data for the pure elements to model the thermodynamics of binary alloy systems: Part 3 – The theoretical prediction of the Al–Si–Zn system,” *Calphad*, vol. 87, p. 102742, Dec. 2024, doi: 10.1016/j.calphad.2024.102742.

[39] E. Zhang, Y. Tang, M. Wen, A. Obaied, I. Roslyakova, and L. Zhang, “On phase stability of Mo-Nb-Ta-W refractory high entropy alloys,” *Int. J. Refract. Met. Hard Mater.*, vol. 103, p. 105780, Feb. 2022, Accessed: Dec. 19, 2025. [Online]. Available: https://www.sciencedirect.com/science/article/pii/S026343682200004X

[40] J.-H. Gao, E.-K. Zhang, Y. Tang, L.-J. Zhang, J. Ding, and X.-C. Xia, “Third-generation

thermodynamic descriptions of MoNbTaWHfZr refractory high entropy alloys and their phase stability," *Tungsten*, vol. 7, no. 3, pp. 582–600, Sep. 2025, doi: 10.1007/s42864-024-00311-y.

[41] J. Ding, J. Gao, E. Zhang, Y. Tang, L. Zhang, and X. Xia, "Thermodynamic Modeling of the Ti-Hf-Zr-Nb-Ta Refractory High Entropy Alloy and Its Application in Analyzing Phase Stability," *Comput. Mater. Contin.*, vol. 85, no. 1, pp. 539–556, 2025, doi: 10.32604/cmc.2025.067266.

[42] R. Otis and Z. Liu, "pycalphad: CALPHAD-based Computational Thermodynamics in Python," *J. Open Res. Softw.*, vol. 5, no. 1, p. 1, Jan. 2017, doi: 10.5334/jors.140.

[43] "PyCalphad: Python library for computational thermodynamics using the CALPHAD method." [Online]. Available: https://pycalphad.org

[44] B. Bocklund, R. Otis, A. Egorov, A. Obaied, I. Roslyakova, and Z.-K. Liu, "ESPEI for efficient thermodynamic database development, modification, and uncertainty quantification: application to Cu–Mg," *MRS Commun.*, vol. 9, no. 2, pp. 618–627, 2019, doi: 10.1557/mrc.2019.59.

[45] "ESPEI: Extensible Self-optimizing Phase Equilibria Infrastructure." [Online]. Available: https://espei.org

[46] Y. Wang, Z. K. Liu, and L. Q. Chen, "Thermodynamic properties of Al, Ni, NiAl, and Ni3Al from first-principles calculations," *Acta Mater.*, vol. 52, no. 9, pp. 2665–2671, May 2004, doi: 10.1016/J.ACTAMAT.2004.02.014.

[47] A. M. Krajewski, J. W. Siegel, J. Xu, and Z.-K. Liu, "Extensible Structure-Informed Prediction of Formation Energy with improved accuracy and usability employing neural networks," *Comput. Mater. Sci.*, vol. 208, p. 111254, 2022, doi:

https://doi.org/10.1016/j.commatsci.2022.111254.

[48] B. Deng *et al.*, "CHGNet as a pretrained universal neural network potential for charge-informed atomistic modelling," *Nat. Mach. Intell.*, vol. 5, no. 9, pp. 1031–1041, Sep. 2023, doi: 10.1038/s42256-023-00716-3.

[49] A. M. Krajewski, J. W. Siegel, and Z. K. Liu, "Efficient structure-informed featurization and property prediction of ordered, dilute, and random atomic structures," *Comput. Mater. Sci.*, vol. 247, p. 113495, Jan. 2025, doi: 10.1016/J.COMMATSCI.2024.113495.

[50] Y. Wang, L. G. Hector, H. Zhang, S. L. Shang, L. Q. Chen, and Z. K. Liu, "Thermodynamics of the Ce γ-α transition: Density-functional study," *Phys. Rev. B*, vol. 78, no. 10, p. 104113, Sep. 2008, doi: 10.1103/PhysRevB.78.104113.

[51] Y. Wang, L. G. Hector, H. Zhang, S. L. Shang, L. Q. Chen, and Z. K. Liu, "A thermodynamic framework for a system with itinerant-electron magnetism," in *Zentropy: Theory and Fundamentals*, Jenny Stanford Publishing, 2024, pp. 539–556. doi: 10.1201/9781032692401-15.

[52] Z.-K. Liu, Y. Wang, and S.-L. Shang, "Zentropy Theory for Positive and Negative Thermal Expansion," in *Zentropy*, vol. 43, no. 6, New York: Jenny Stanford Publishing, 2024, pp. 497–514. doi: 10.1201/9781032692401-13.

[53] Z.-K. Liu, "Quantitative predictive theories through integrating quantum, statistical, equilibrium, and nonequilibrium thermodynamics," *J. Phys. Condens. Matter*, vol. 36, no. 34, p. 343003, Aug. 2024, doi: 10.1088/1361-648X/ad4762.

[54] F. Tang and B. Hallstedt, "Using the PARROT module of Thermo-Calc with the Cr–Ni system as example," *Calphad*, vol. 55, pp. 260–269, Dec. 2016, doi: 10.1016/j.calphad.2016.10.003.

[55] Z. K. Liu, “Ocean of Data: Integrating First-Principles Calculations and CALPHAD Modeling with Machine Learning,” *J. Phase Equilibria Diffus.*, vol. 39, no. 5, pp. 635–649, Oct. 2018, doi: 10.1007/S11669-018-0654-Z/FIGURES/8.

[56] B. Wilthan, “NIST alloy data,” National Institute of Standards and Technology. Accessed: Nov. 03, 2024. [Online]. Available: https://doi.org/10.18434/M32153

[57] G. Grimvall, *Thermophysical properties of materials*. Elsevier, 1999.

[58] M. Hillert and M. Jarl, “A model for alloying in ferromagnetic metals,” *Calphad*, vol. 2, no. 3, pp. 227–238, Jan. 1978, doi: 10.1016/0364-5916(78)90011-1.

[59] W. Xiong, Q. Chen, P. A. Korzhavyi, and M. Selleby, “An improved magnetic model for thermodynamic modeling,” *Calphad*, vol. 39, pp. 11–20, 2012, doi: https://doi.org/10.1016/j.calphad.2012.07.002.

[60] A. Gelman, J. B. Carlin, H. S. Stern, and D. B. Rubin, *Bayesian data analysis*. Chapman and Hall/CRC, 1995.

[61] N. H. Paulson, B. J. Bocklund, R. A. Otis, Z.-K. Liu, and M. Stan, “Quantified uncertainty in thermodynamic modeling for materials design,” *Acta Mater.*, vol. 174, pp. 9–15, 2019, doi: https://doi.org/10.1016/j.actamat.2019.05.017.

[62] N. H. Paulson, S. Zomorodpoosh, I. Roslyakova, and M. Stan, “Comparison of statistically-based methods for automated weighting of experimental data in CALPHAD-type assessment,” *Calphad*, vol. 68, p. 101728, 2020, doi: https://doi.org/10.1016/j.calphad.2019.101728.

[63] J. E. Cavanaugh, “Unifying the derivations for the Akaike and corrected Akaike information criteria,” *Stat. Probab. Lett.*, vol. 33, no. 2, pp. 201–208, 1997, doi: 10.1016/s0167-7152(96)00128-9.

[64] K. P. Burnham and D. R. Anderson, “Multimodel inference: Understanding AIC and BIC in model selection,” 2004, *Sage Publications Sage CA: Thousand Oaks, CA*. doi: 10.1177/0049124104268644.

[65] A. Obaied *et al.*, “Thermodynamic re-assessment of pure chromium using modified segmented regression model,” *Calphad*, vol. 69, p. 101762, Jun. 2020, doi: 10.1016/j.calphad.2020.101762.

[66] A. Richter, “PureElementPRL,” Jan. 09, 2026, *GitHub*. [Online]. Available: https://github.com/amr8004/PureElementPRL

[67] C. Kittel, *Introduction to Solid State Physics*, 8th ed. New York, NY: John Wiley & Sons, 2005.

[68] S. Bigdeli *et al.*, “An insight into using DFT data for Calphad modeling of solid phases in the third generation of Calphad databases, a case study for Al,” *Calphad*, vol. 65, pp. 79–85, Jun. 2019, doi: 10.1016/j.calphad.2019.02.008.

[69] R. Gong *et al.*, “Thermodynamic modeling of the LiCl-KCl-LaCl3 system with Bayesian model selection and uncertainty quantification,” *J. Mol. Liq.*, vol. 432, p. 127811, Aug. 2025, doi: 10.1016/J.MOLLIQ.2025.127811.

## 11.1 Figures

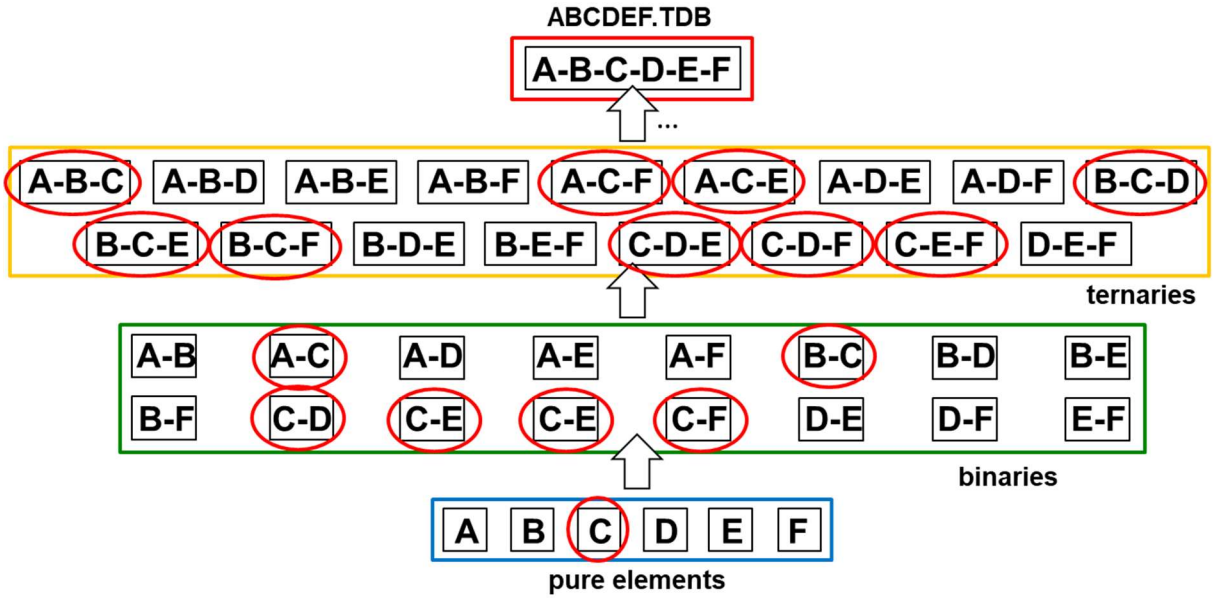


*Figure 1 Circled systems to be remodeled in a hypothetical 6 element database of A-B-C-D-E-F, if the thermodynamic description of pure Element "C" is modified, reproduced from Ref.* [13].

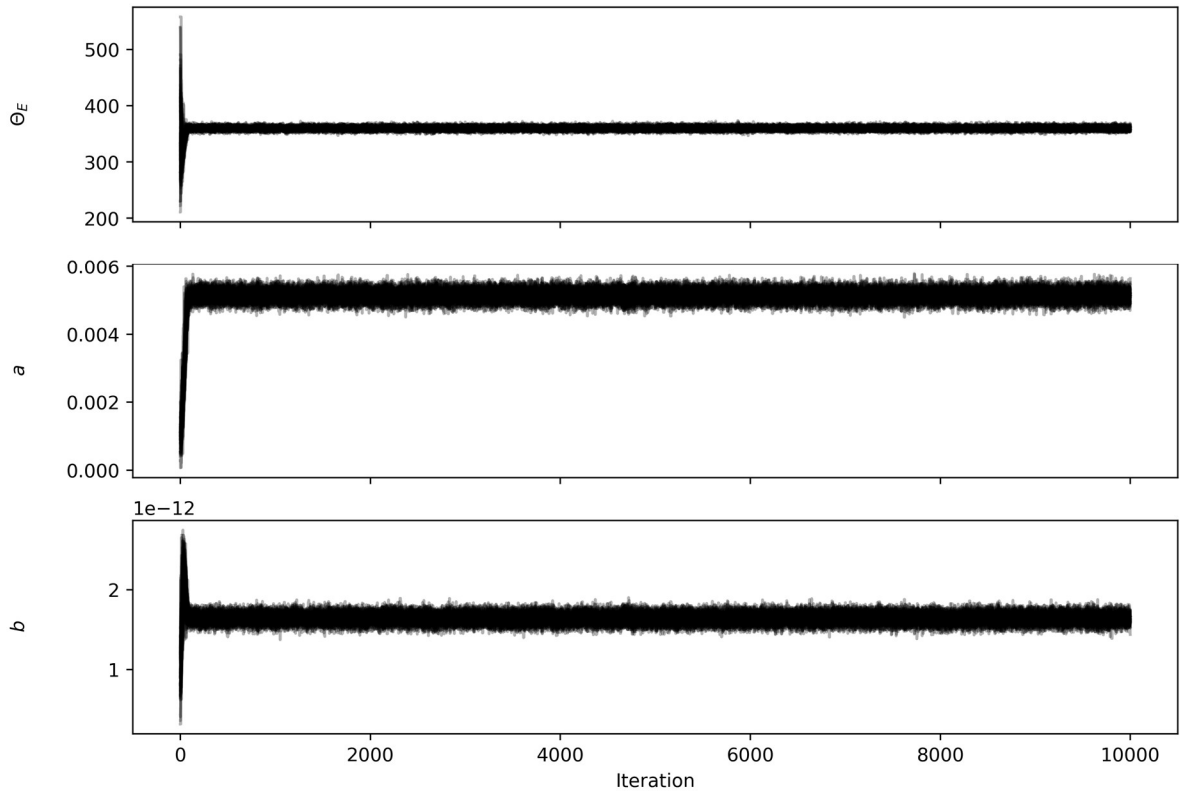
$\Theta_E$
500
400
300
200
$a$
0.006
0.004
0.002
0.000
1e−12
$b$
2
1
0
2000
4000
6000
8000
10000
Iteration

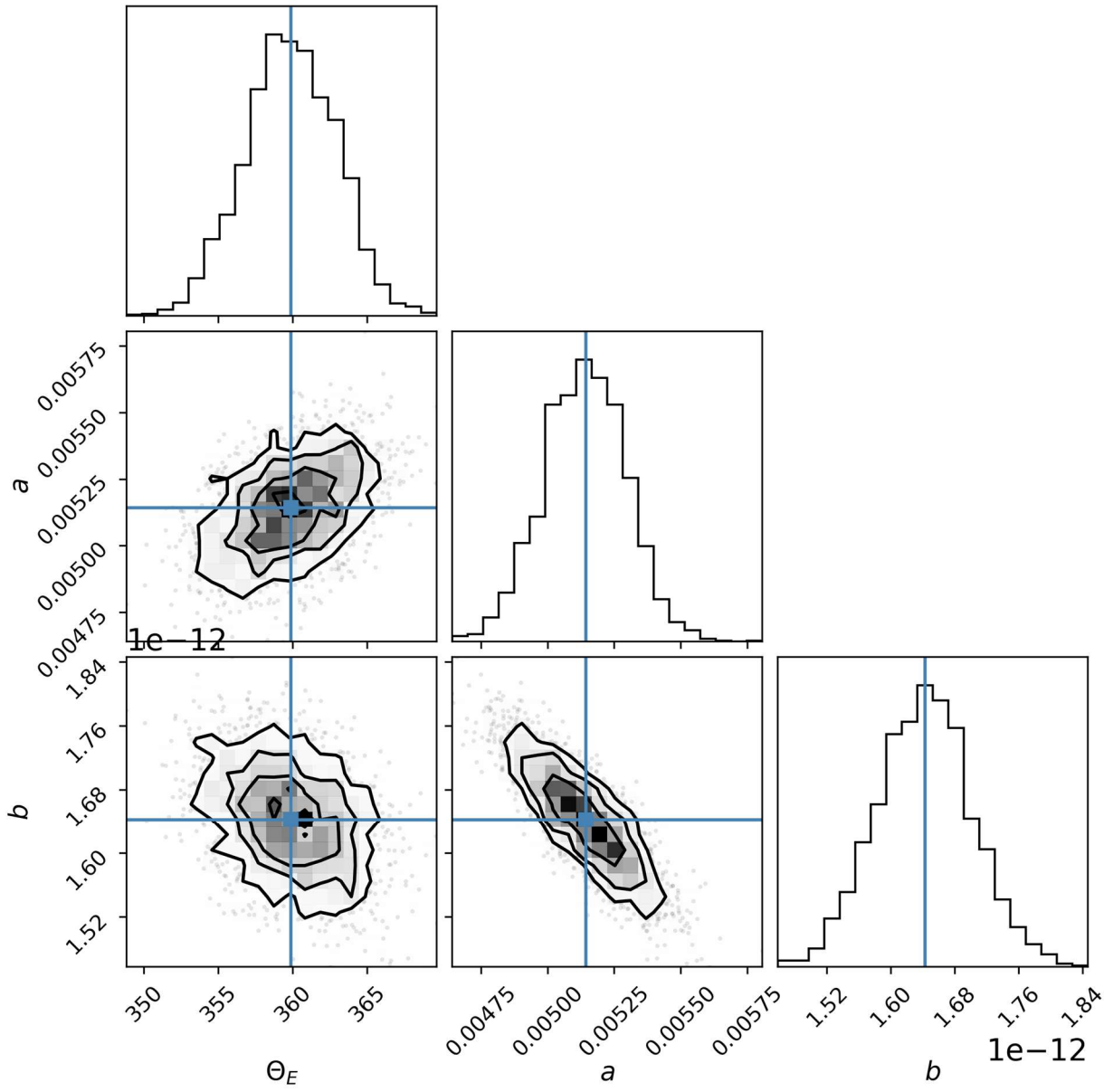


*Figure 2 Convergence of MCMC chains for parameters $\theta_E$, a, and b (top) and the corresponding corner plot (bottom) showing posterior distributions and parameter correlations for Cr using the CS model.*

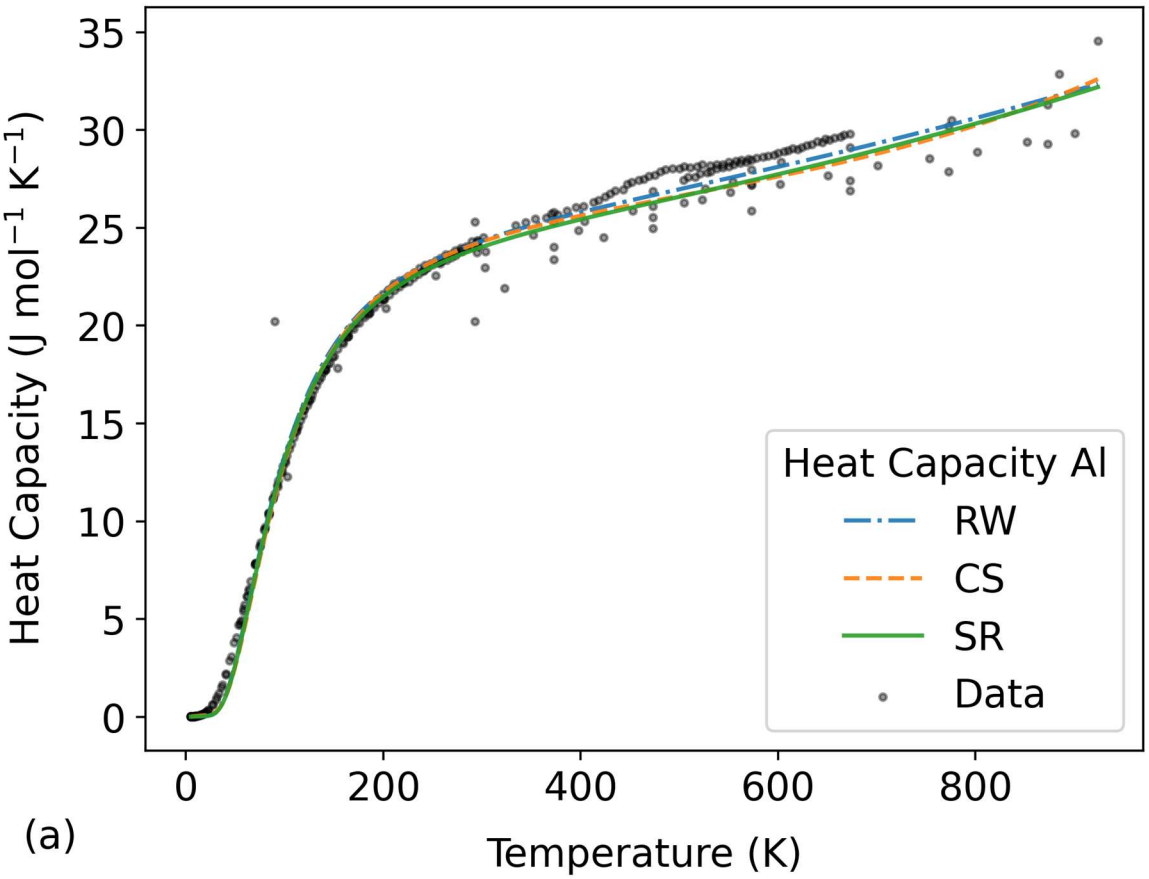
Heat Capacity (J mol$^{-1}$ K$^{-1}$)
35
30
25
20
15
10
5
0
0
200
400
600
800
Temperature (K)
Heat Capacity Al
RW
CS
SR
Data

(a)

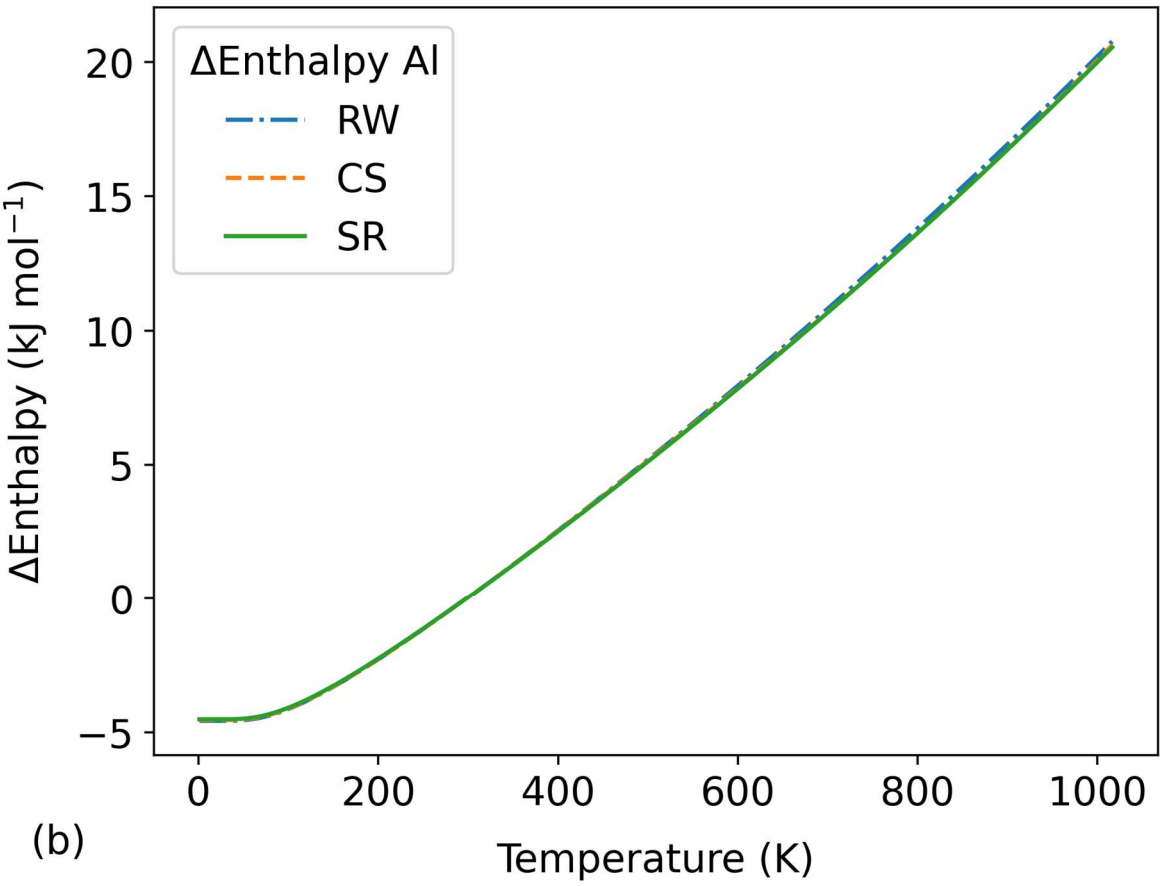
ΔEnthalpy Al
RW
CS
SR
ΔEnthalpy (kJ mol⁻¹)
20
15
10
5
0
−5
0
200
400
600
800
1000
Temperature (K)

(b)

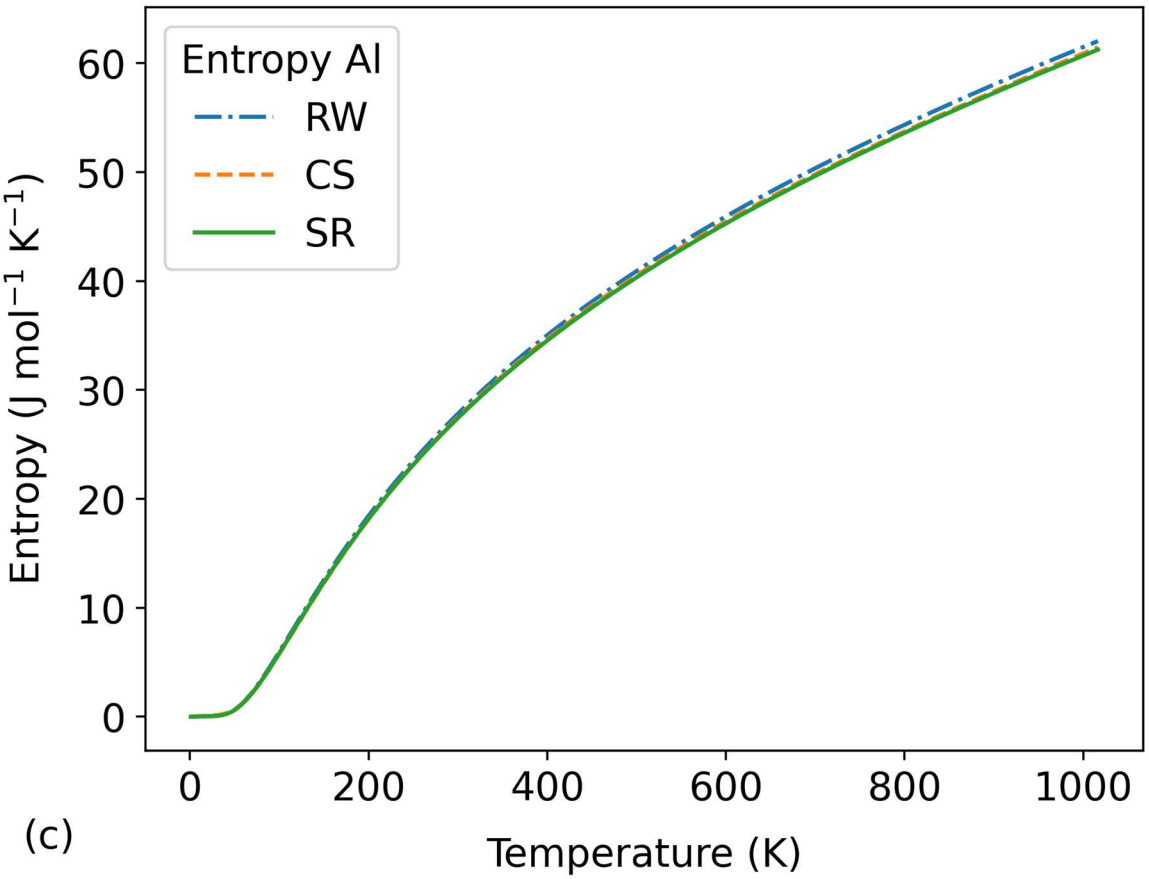
Entropy Al
RW
CS
SR
Entropy (J mol$^{-1}$ K$^{-1}$)
Temperature (K)
0
10
20
30
40
50
60
0
200
400
600
800
1000

(c)

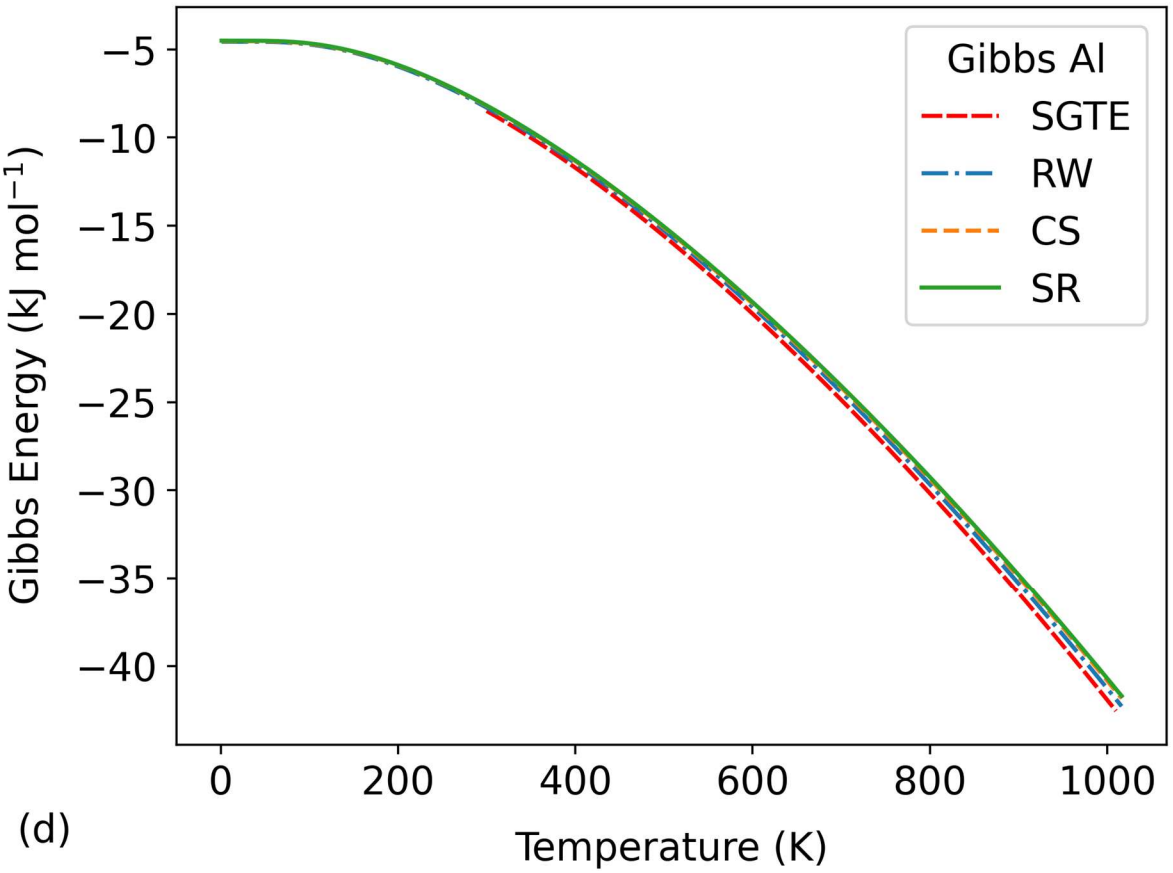
Gibbs Al
SGTE
RW
CS
SR
Gibbs Energy (kJ mol$^{-1}$)
−5
−10
−15
−20
−25
−30
−35
−40
0
200
400
600
800
1000
Temperature (K)

(d)

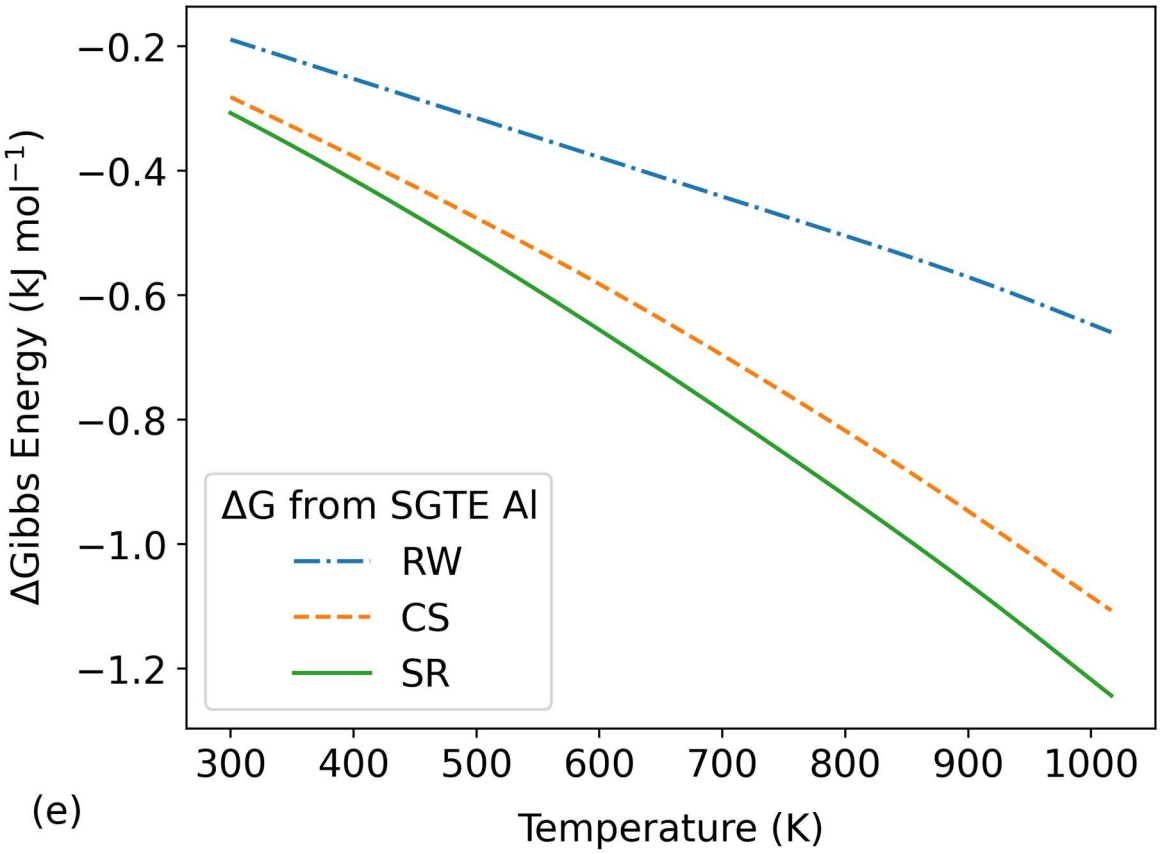


*Figure 3 Thermodynamic properties of Al with three models: (a) Heat capacity with experimental data superimposed; (b) ΔEnthalpy, (c), Entropy, (d) Gibbs energy, and (e) Gibbs energy difference with respect to the SGTE91 database.*

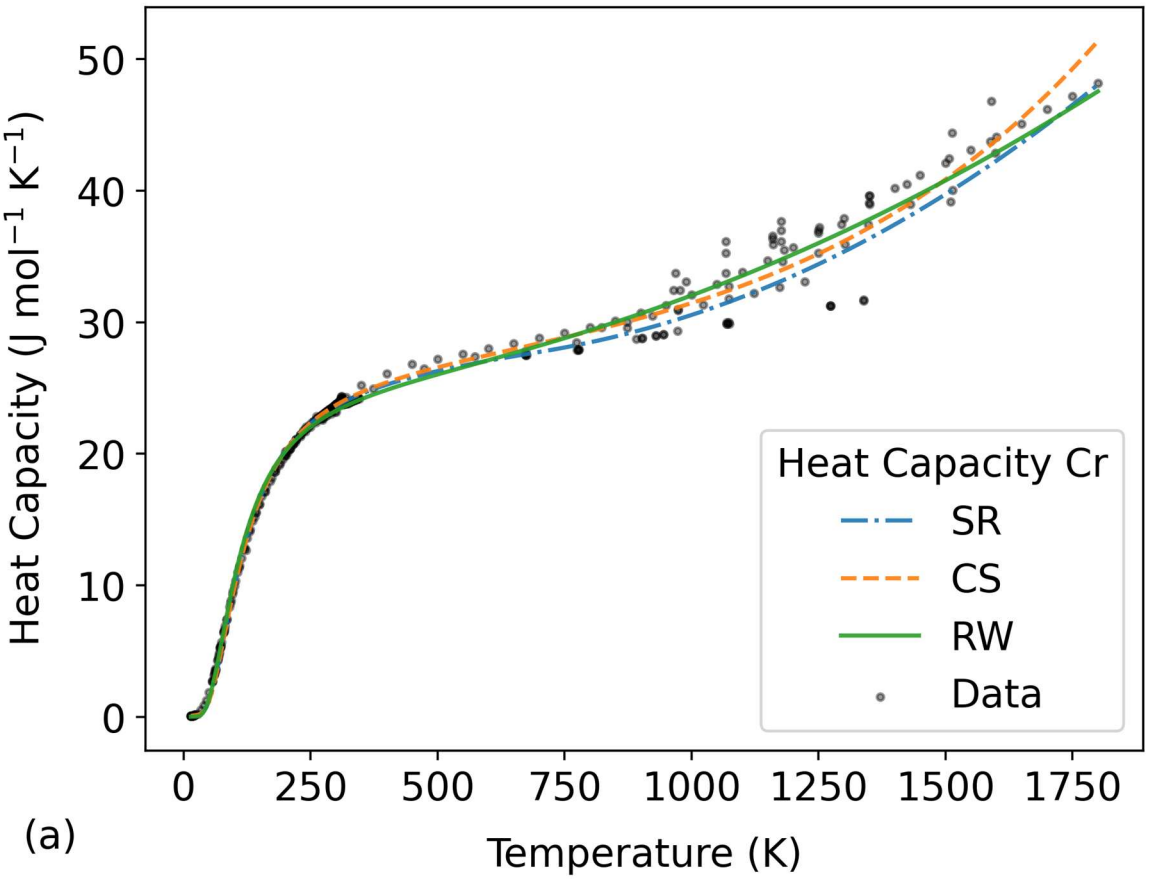
Heat Capacity (J mol$^{-1}$ K$^{-1}$)
50
40
30
20
10
0
0
250
500
750
1000
1250
1500
1750
Temperature (K)
Heat Capacity Cr
SR
CS
RW
Data

(a)

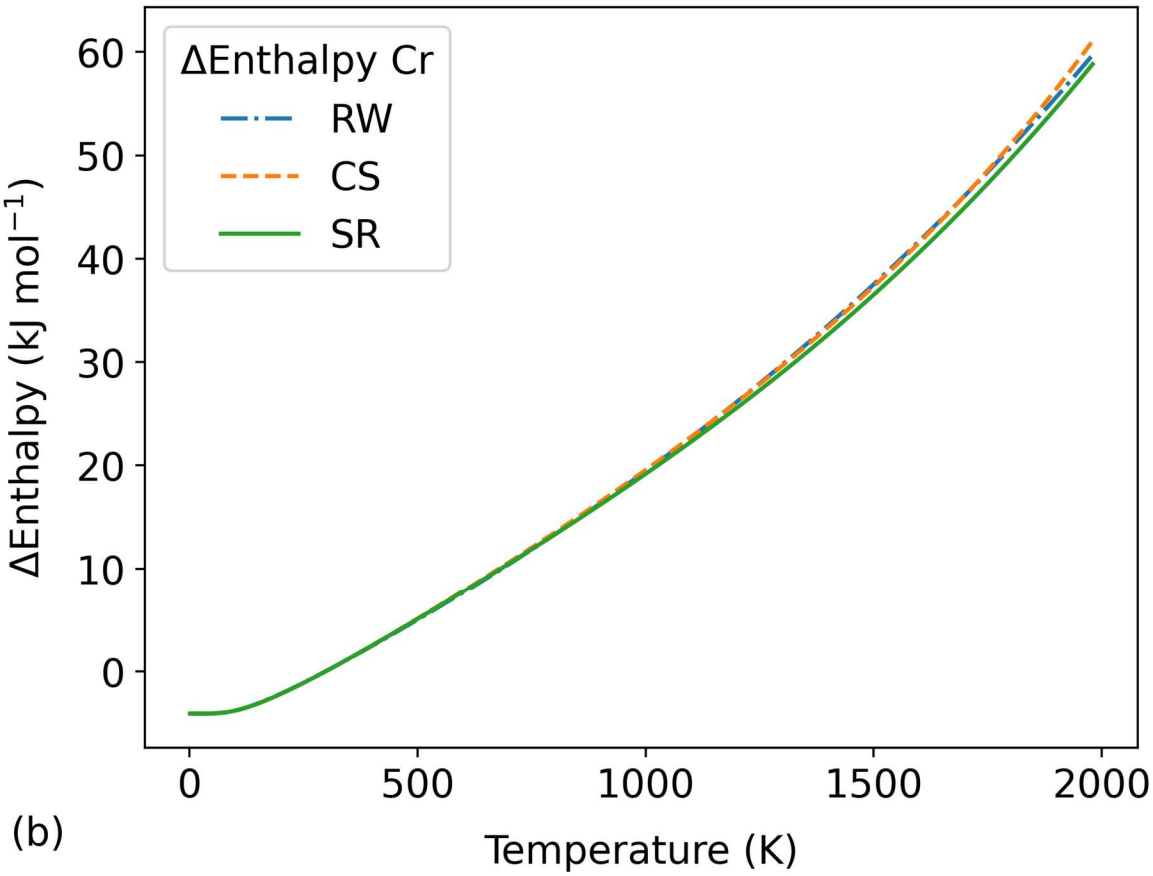
ΔEnthalpy Cr
RW
CS
SR
ΔEnthalpy (kJ mol⁻¹)
60
50
40
30
20
10
0
0
500
1000
1500
2000
Temperature (K)

(b)

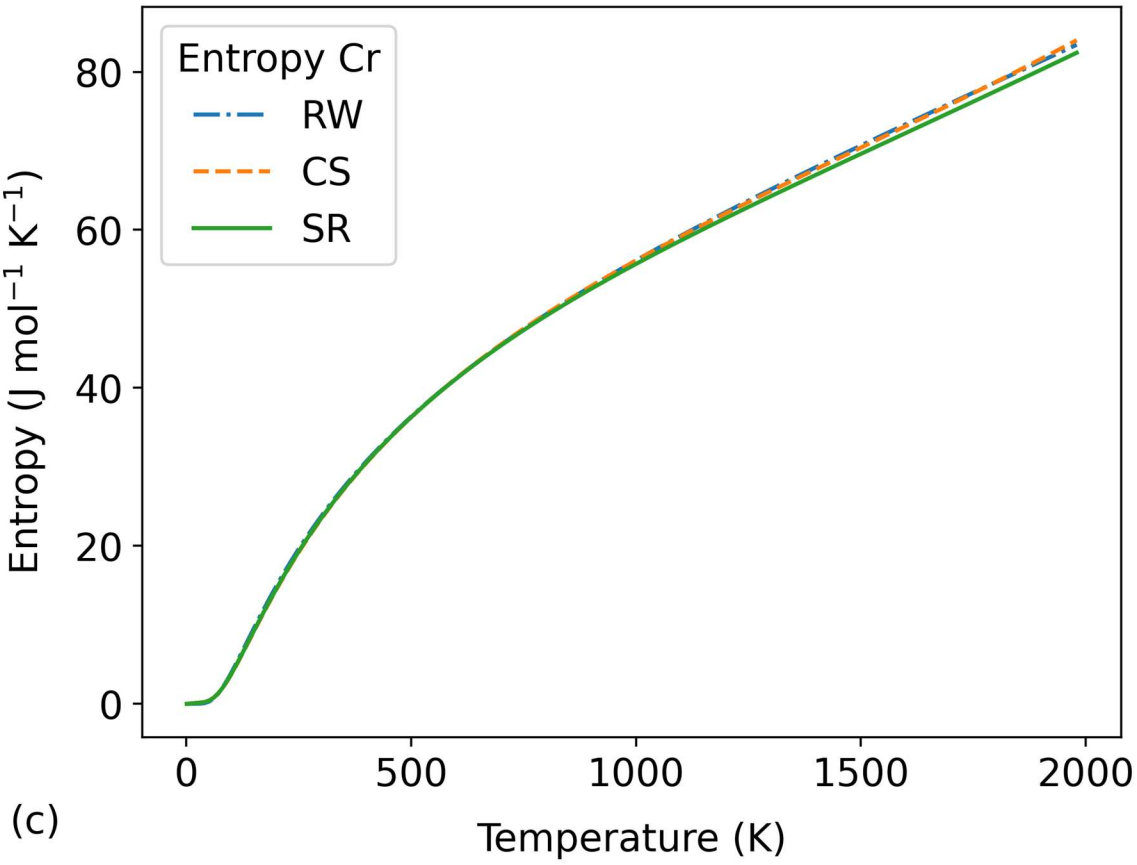
Entropy Cr
RW
CS
SR
Entropy (J mol$^{-1}$ K$^{-1}$)
Temperature (K)
0
20
40
60
80
0
500
1000
1500
2000

(c)

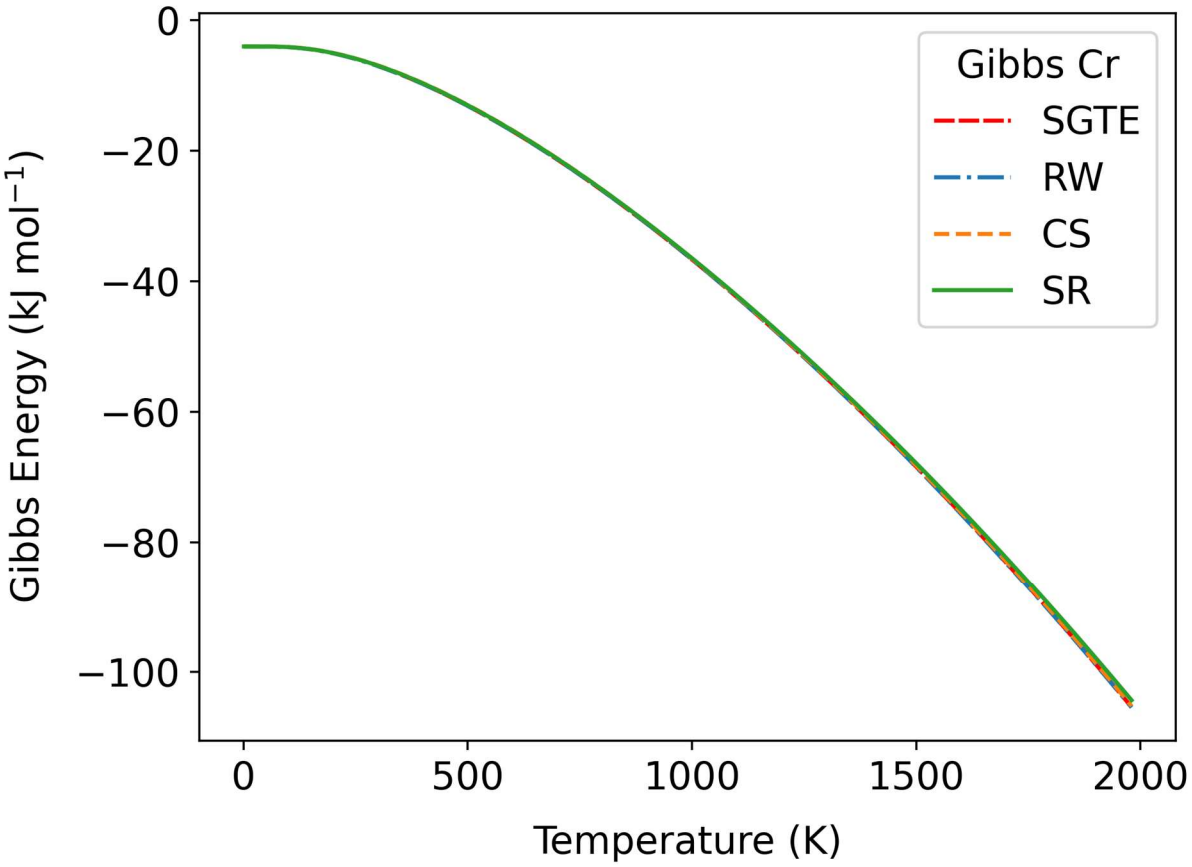
Gibbs Cr
SGTE
RW
CS
SR
Gibbs Energy (kJ mol$^{-1}$)
Temperature (K)
0
−20
−40
−60
−80
−100
0
500
1000
1500
2000

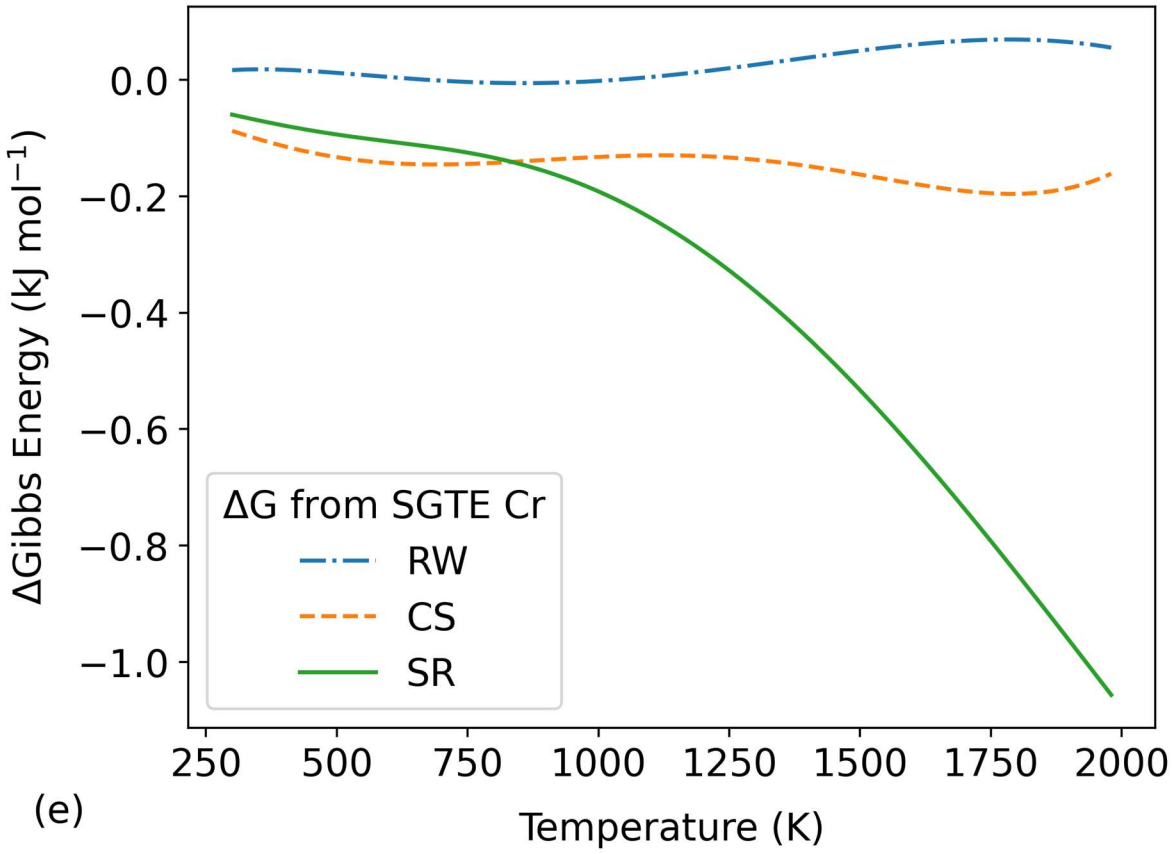


*Figure 4 Thermodynamic properties of Cr with three models: (a) Heat capacity with experimental data superimposed; (b) ΔEnthalpy, (c) Entropy, (d) Gibbs energy, and (e) Gibbs energy difference with respect to the SGTE91 database.*

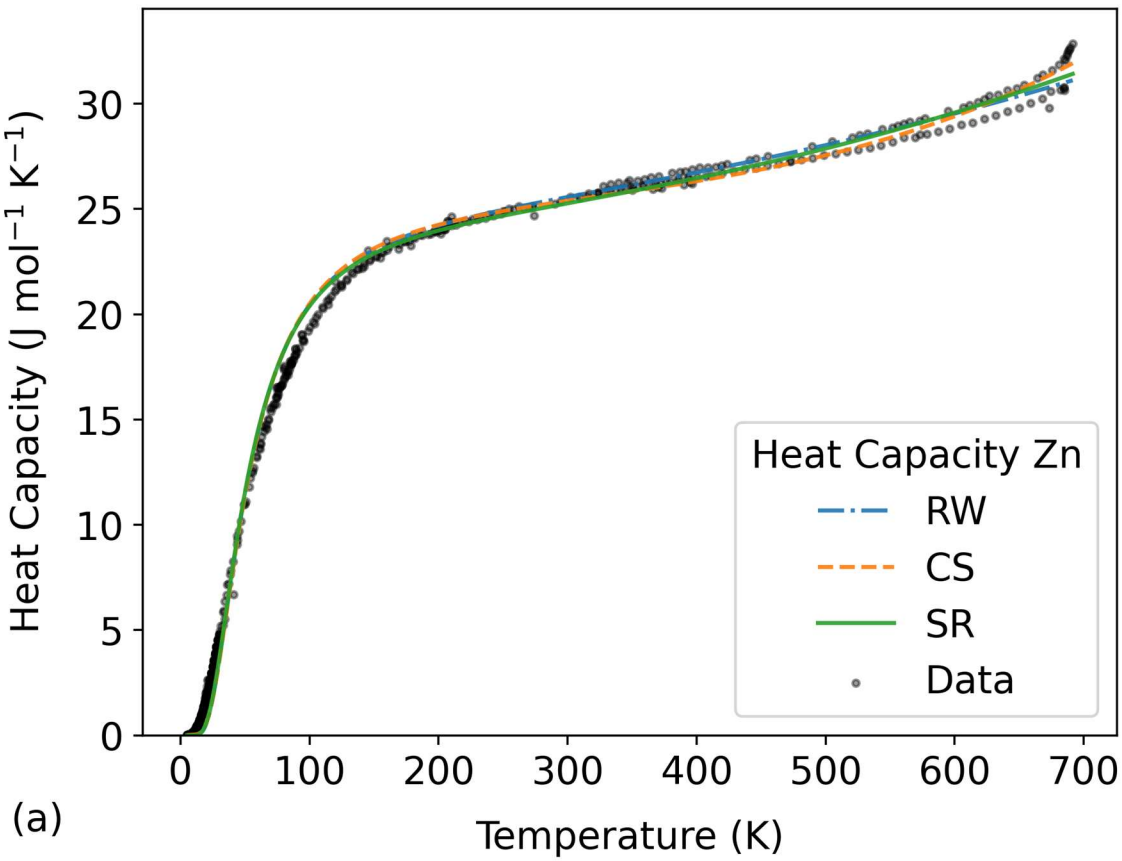
Heat Capacity (J mol$^{-1}$ K$^{-1}$)
0
5
10
15
20
25
30
0
100
200
300
400
500
600
700
Temperature (K)
Heat Capacity Zn
RW
CS
SR
Data

(a)

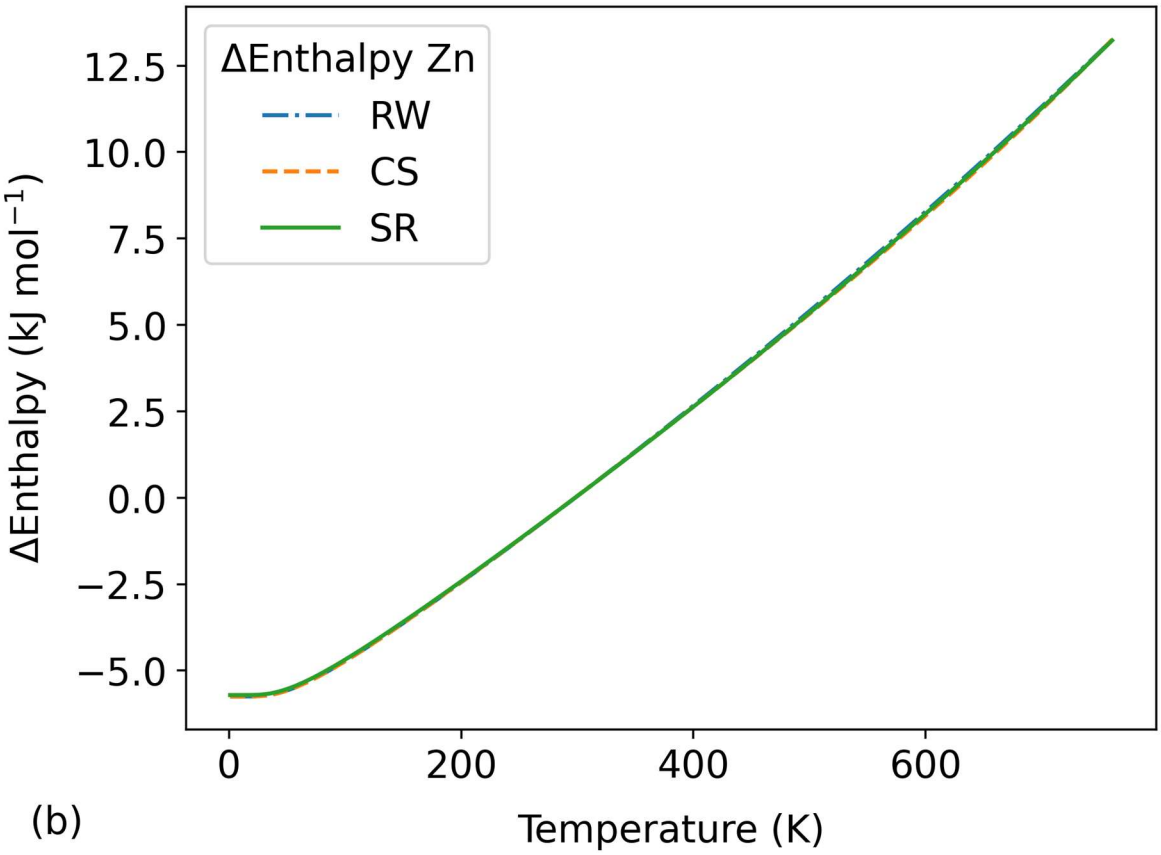
ΔEnthalpy Zn
RW
CS
SR
12.5
10.0
7.5
5.0
2.5
0.0
−2.5
−5.0
ΔEnthalpy (kJ mol$^{-1}$)
0
200
400
600
Temperature (K)

(b)

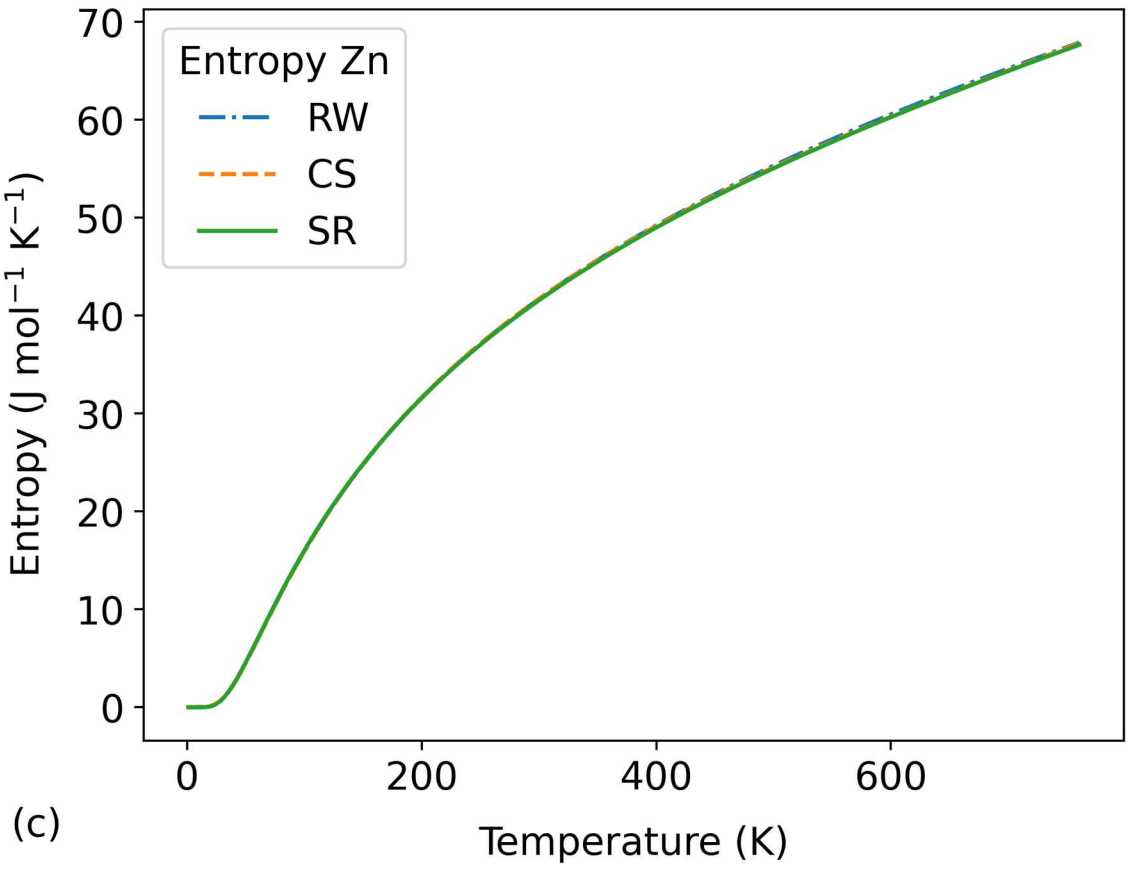
Entropy Zn
RW
CS
SR
Entropy (J mol$^{-1}$ K$^{-1}$)
Temperature (K)
0
10
20
30
40
50
60
70
0
200
400
600

(c)

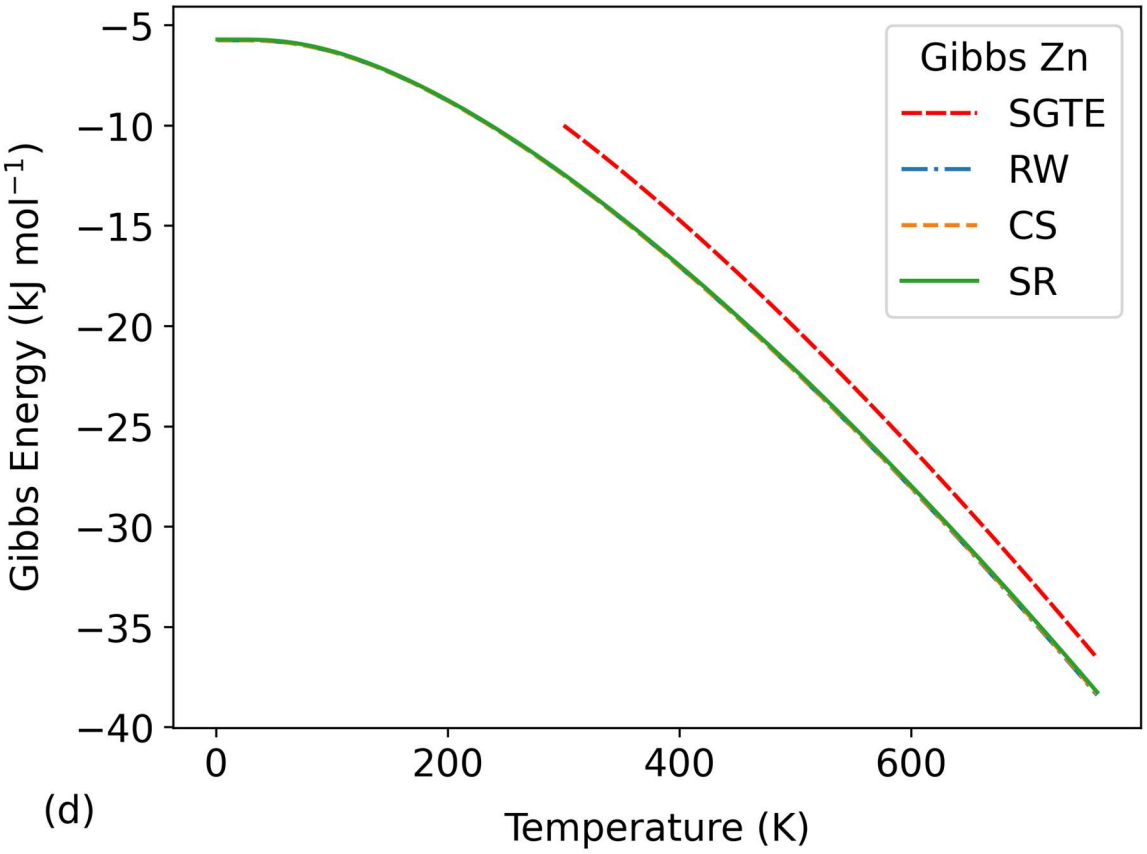
Gibbs Zn
SGTE
RW
CS
SR
−5
−10
−15
−20
−25
−30
−35
−40
Gibbs Energy (kJ mol$^{-1}$)
0
200
400
600
Temperature (K)
(d)

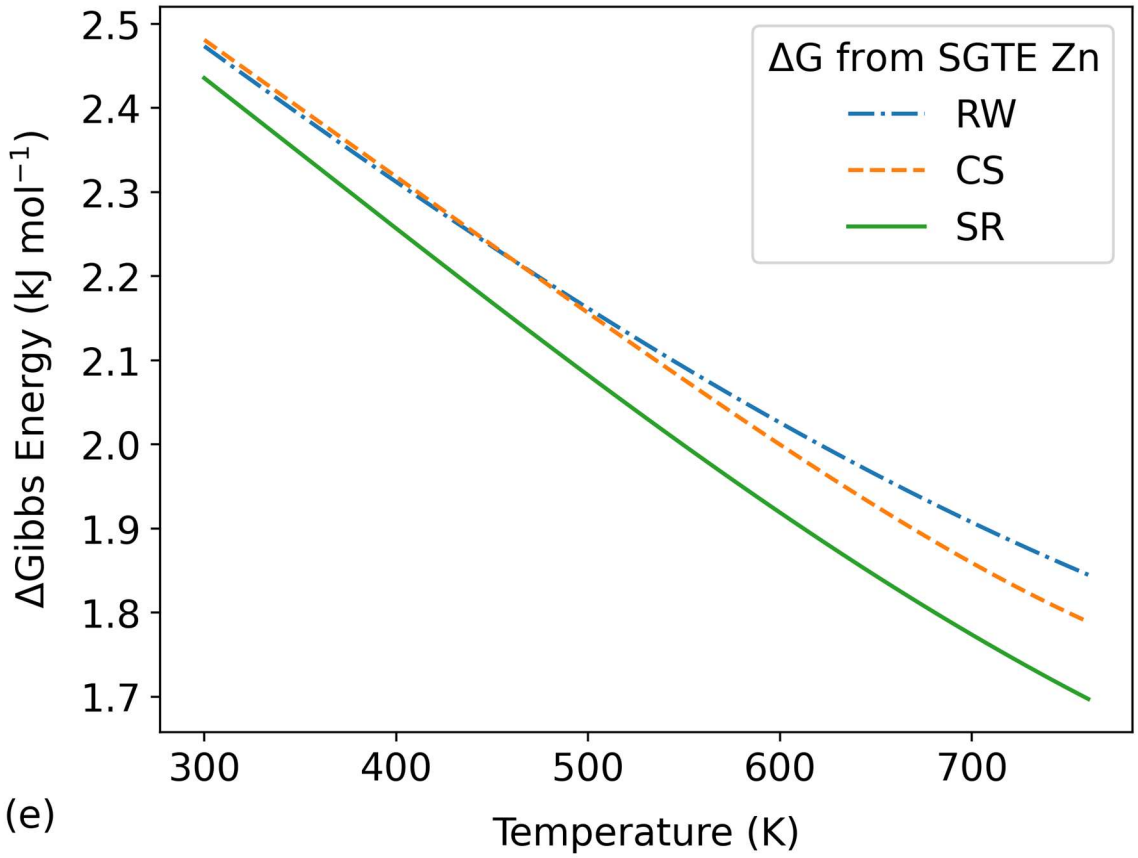


*Figure 5 Thermodynamic properties of Zn with three models: (a) Heat capacity with experimental data superimposed; (b) ΔEnthalpy, (c) Entropy, (d) Gibbs energy, and (e) Gibbs energy difference with respect to the SGTE91 database*

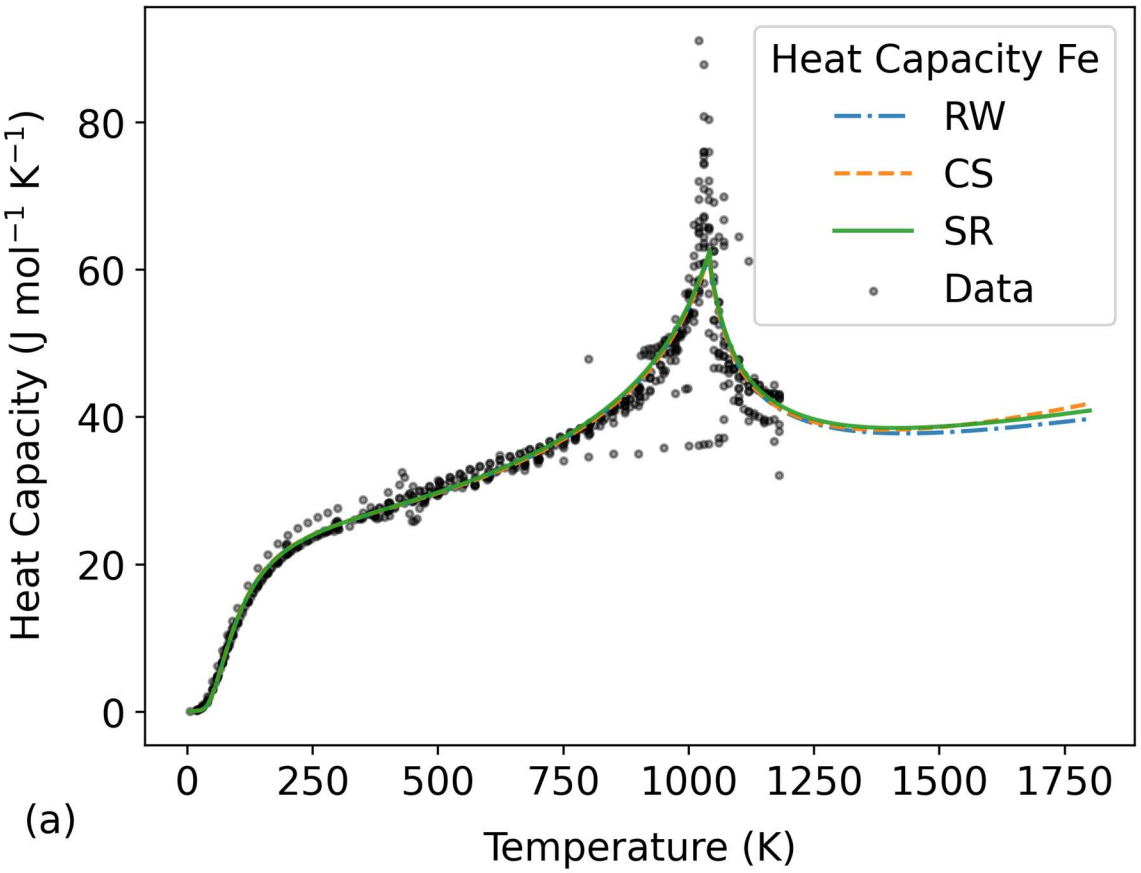
Heat Capacity Fe
RW
CS
SR
Data
Heat Capacity (J mol$^{-1}$ K$^{-1}$)
0
20
40
60
80
0
250
500
750
1000
1250
1500
1750
Temperature (K)
(a)

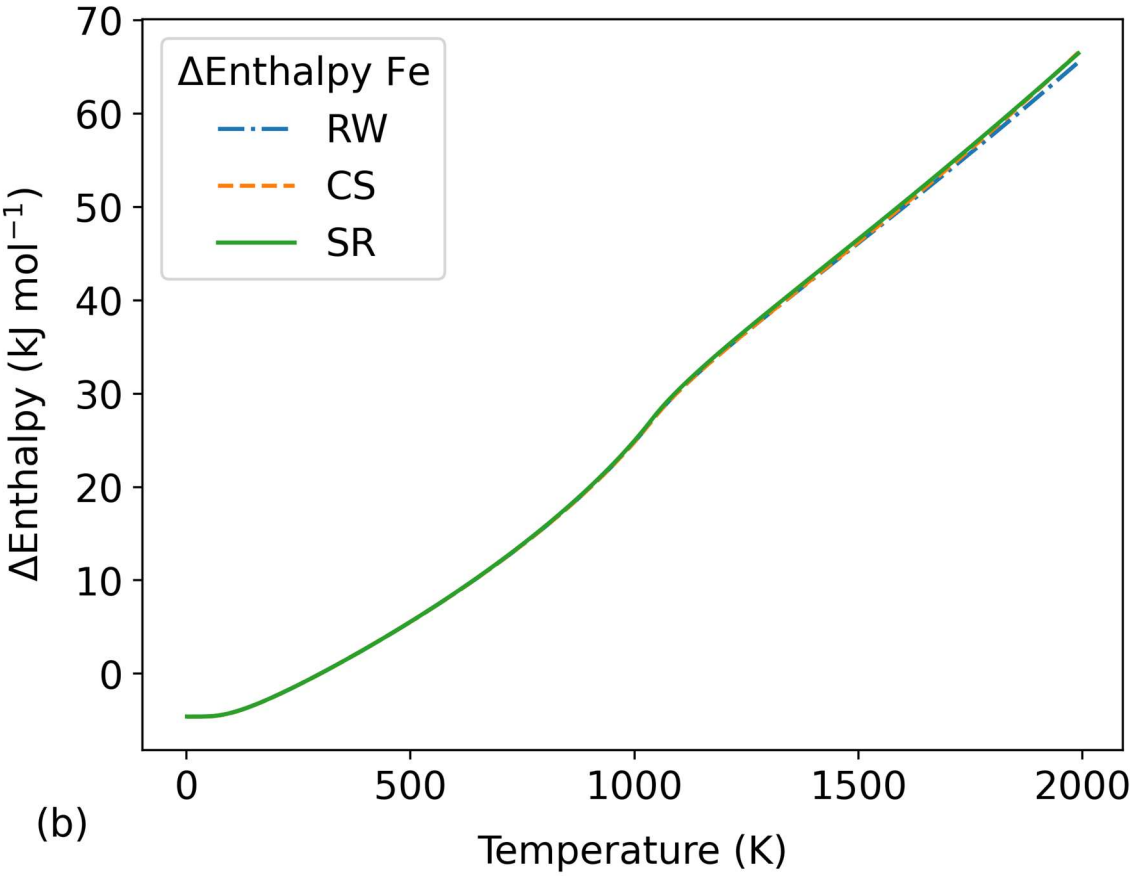
ΔEnthalpy Fe
RW
CS
SR
ΔEnthalpy (kJ mol⁻¹)
Temperature (K)
0
10
20
30
40
50
60
70
0
500
1000
1500
2000

(b)

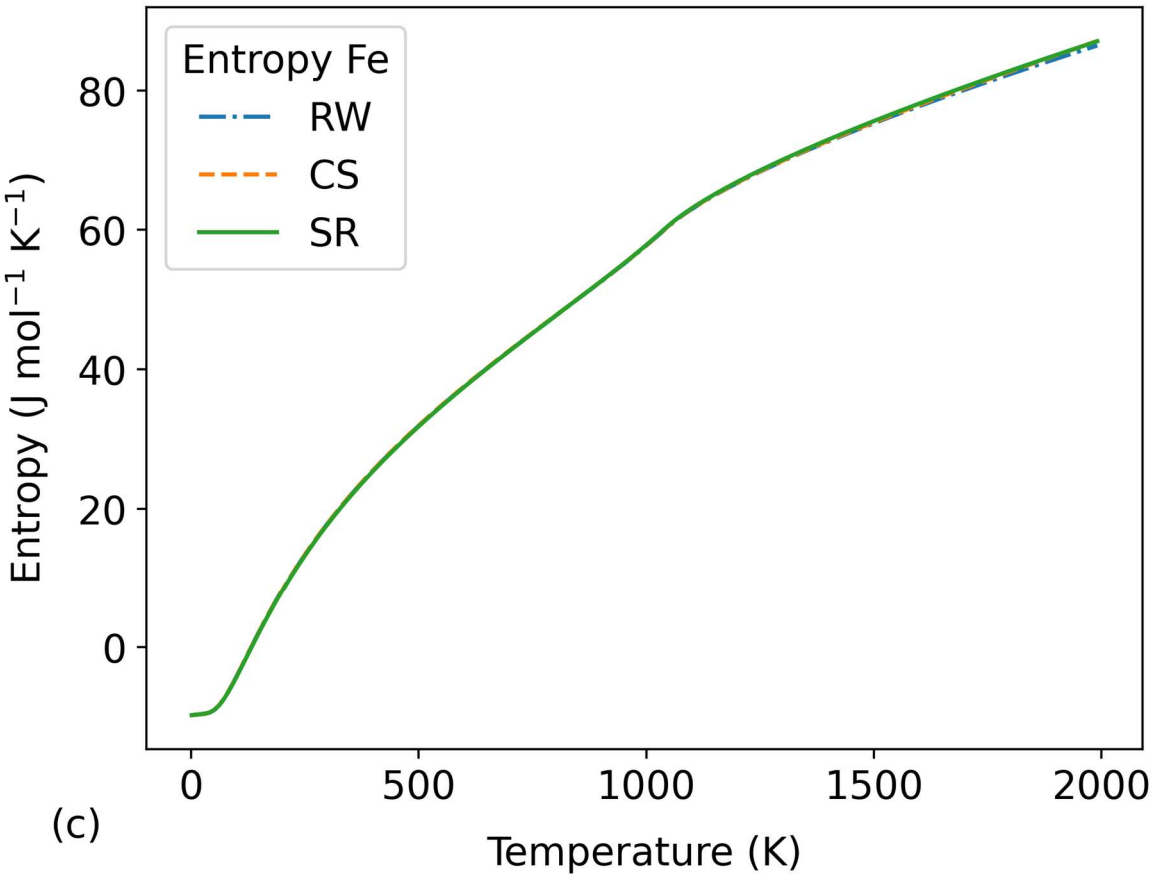
Entropy Fe
RW
CS
SR
Entropy (J mol$^{-1}$ K$^{-1}$)
80
60
40
20
0
0
500
1000
1500
2000
Temperature (K)

(c)

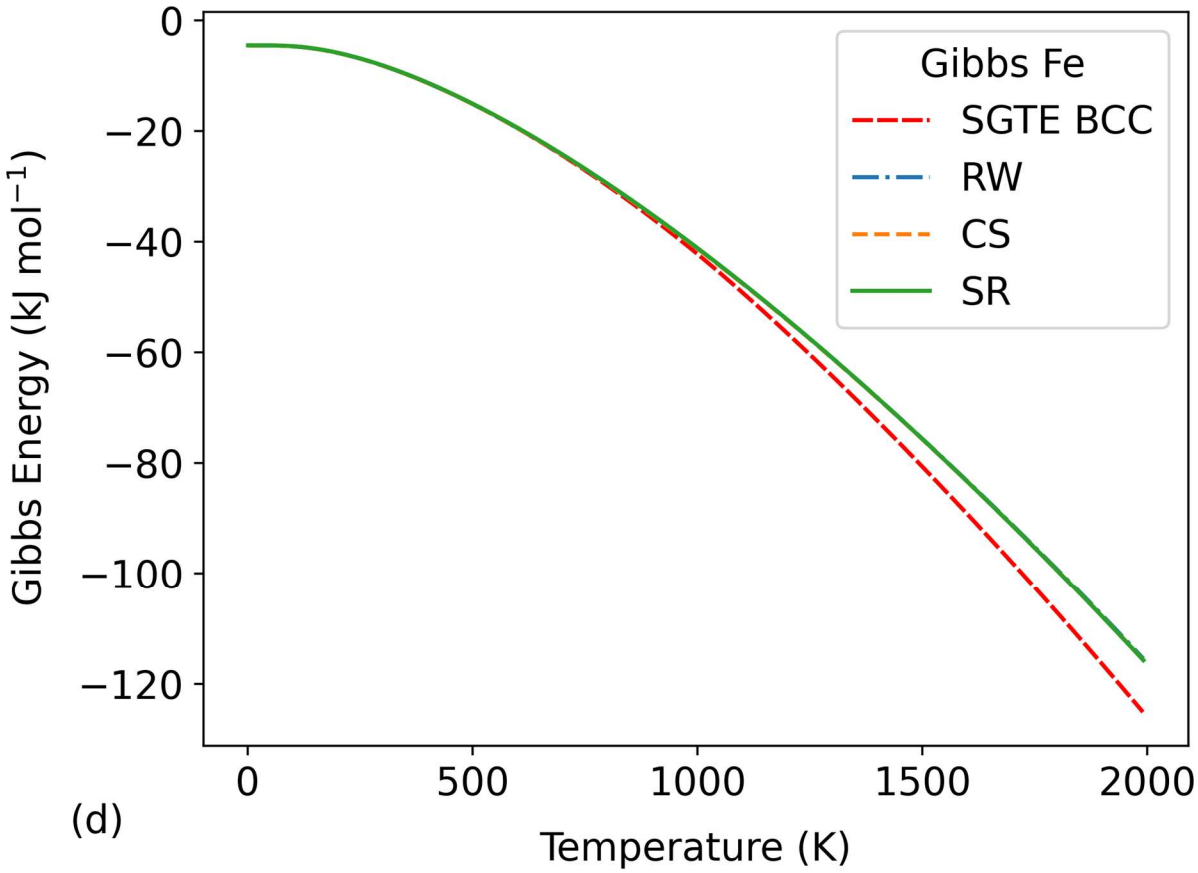
Gibbs Fe
SGTE BCC
RW
CS
SR
0
−20
−40
−60
−80
−100
−120
Gibbs Energy (kJ mol$^{-1}$)
0
500
1000
1500
2000
Temperature (K)
(d)

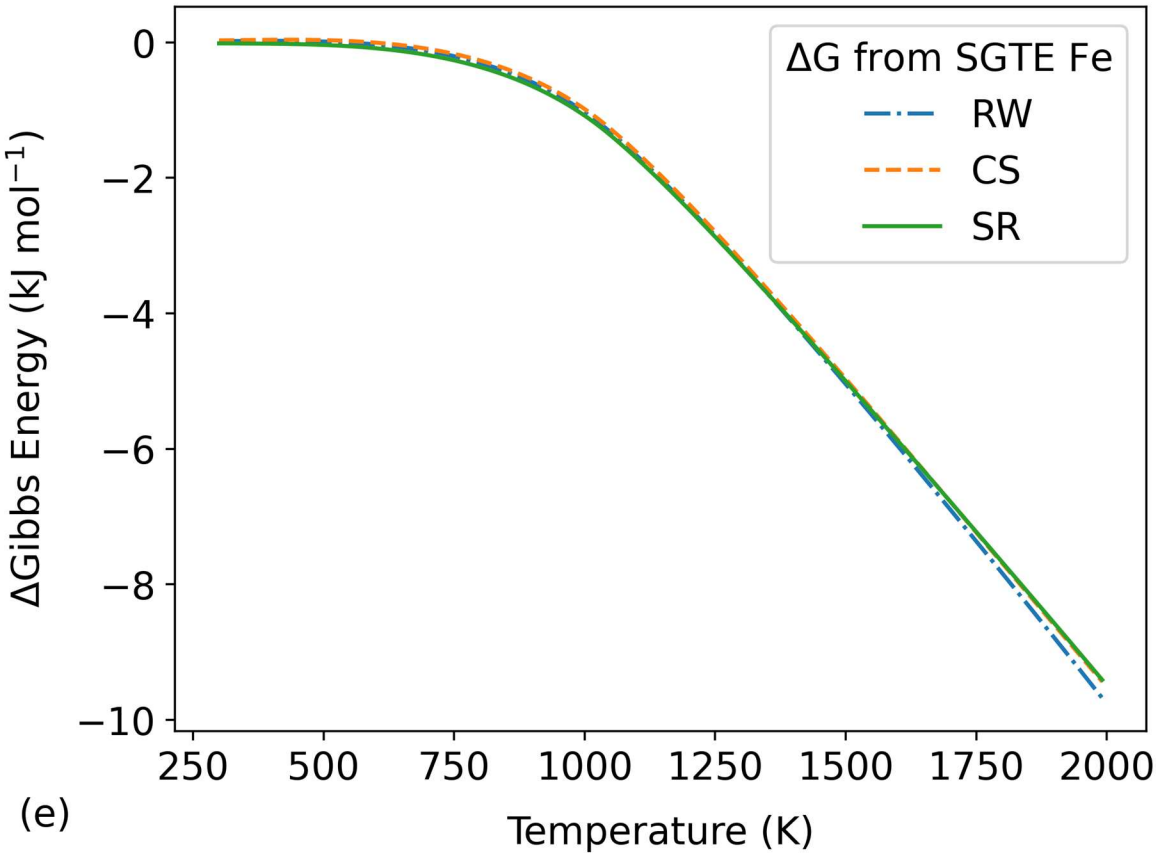


*Figure 6 Thermodynamic properties of Fe with three models: (a) Heat capacity with experimental data superimposed; (b) ΔEnthalpy, (c) Entropy, (d) Gibbs energy, and (e) Gibbs energy difference with respect to the SGTE91 database*

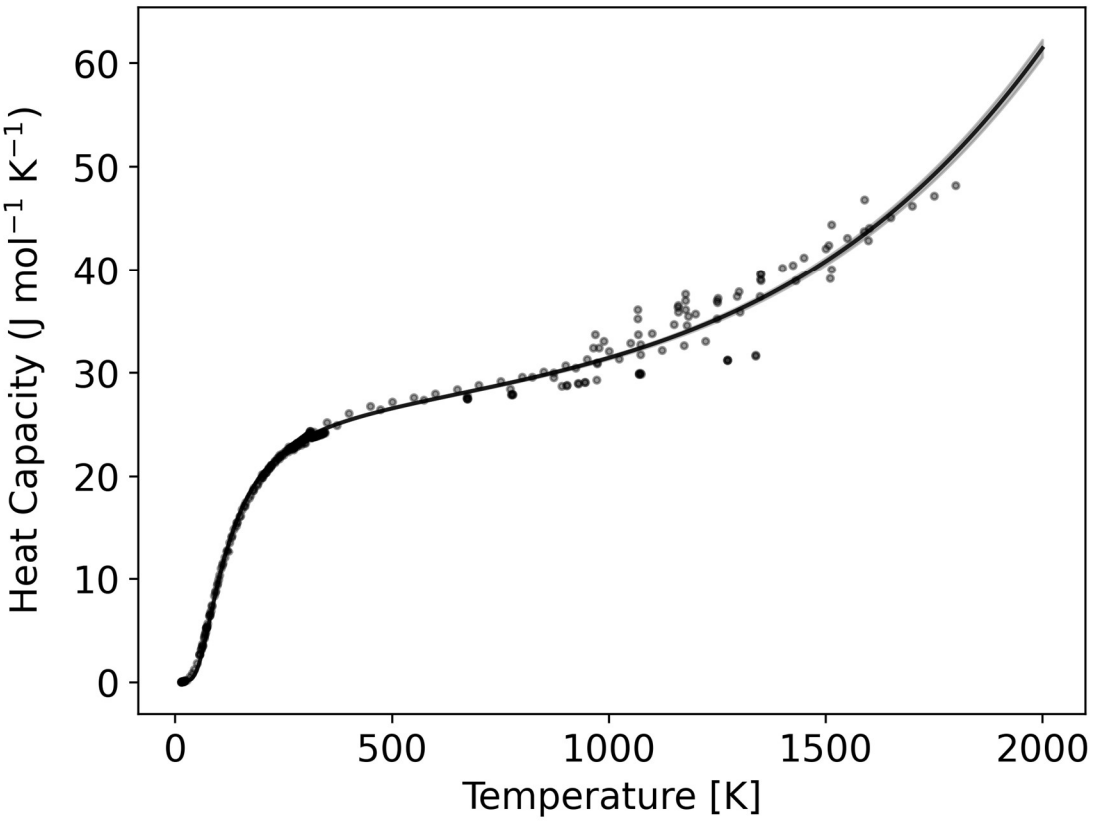


*Figure 7 Heat capacity of BCC Cr from the CS model with uncertainty propagated from retained MCMC samples. The black line shows the highest likelihood parameter, and the gray region shows the range of predictions generated from the posterior samples.*

*Table 1 Einstein parameter $\theta_E$ in kelvin evaluated for three models and compared to $\theta_E$ recalculated from $\theta_E \cong 0.77\theta_D$ [57] collected from Kittel* [67]

| Element | RW Model | CS Model | SR Model | Kittel |
|---|---|---|---|---|
| Ag | 152.663 | 154.105 | 157.126 | 161.220 |
| Al | 288.481 | 294.657 | 293.643 | 306.675 |
| As | 216.932 | 216.045 | 216.093 | 202.062 |
| Au | 119.064 | 119.984 | 118.060 | 118.228 |
| Be | 693.977 | 692.600 | 691.488 | 1031.805 |
| Bi | 79.841 | 79.786 | 80.281 | 85.267 |
| Ca | 167.673 | 168.106 | 168.601 | 164.802 |
| Cd | 105.736 | 106.342 | 105.181 | 149.755 |
| Co | 276.916 | 276.925 | 310.849 | 318.856 |
| Cr | 337.775 | 357.353 | 356.820 | 451.415 |
| Cs | 32.696 | 33.159 | 33.567 | 27.228 |
| Cu | 233.121 | 235.063 | 235.628 | 252.936 |
| Fe | 302.647 | 305.513 | 308.012 | 336.770 |
| Ge | 252.417 | 251.854 | 251.884 | 267.983 |
| Hf | 148.562 | 148.734 | 151.373 | 180.566 |
| Hg | 67.104 | 66.658 | 68.912 | 51.519 |
| Ir | 213.588 | 213.811 | 214.048 | 300.943 |
| K | 70.806 | 71.599 | 73.002 | 65.204 |
| La | 86.838 | 86.627 | 87.366 | 101.747 |
| Mg | 238.898 | 243.708 | 236.739 | 286.613 |
| Mn | 303.819 | 304.932 | 311.649 | 293.778 |
| Mo | 273.099 | 287.375 | 286.843 | 322.439 |
| Na | 119.313 | 120.402 | 118.284 | 113.212 |
| Nb | 202.714 | 209.529 | 203.953 | 197.046 |
| Ni | 275.288 | 282.830 | 272.713 | 322.439 |
| Pb | 62.947 | 63.204 | 65.597 | 75.236 |
| Pd | 202.244 | 203.136 | 210.445 | 196.330 |
| Pt | 172.192 | 173.854 | 173.836 | 171.968 |
| Rb | 4.551 | 46.211 | 47.278 | 40.126 |
| Re | 194.074 | 196.270 | 198.906 | 308.108 |
| Rh | 253.896 | 255.783 | 256.389 | 343.935 |
| Sb | 134.463 | 135.949 | 136.153 | 151.188 |
| Sc | 224.294 | 231.820 | 230.018 | 257.951 |
| Si | 456.413 | 457.542 | 454.617 | 462.163 |

| | | | | |
|---|---|---|---|---|
| Sn | 121.411 | 123.778 | 121.459 | 143.306 |
| Ta | 163.756 | 166.897 | 166.724 | 171.968 |
| Tl | 67.302 | 67.451 | 67.537 | 56.248 |
| V | 273.551 | 279.449 | 281.809 | 272.282 |
| W | 229.228 | 231.816 | 235.770 | 286.613 |
| Y | 146.363 | 147.039 | 154.774 | 200.629 |
| Zn | 158.841 | 160.560 | 157.789 | 234.306 |

*Table 2 AICc values of RW, CS and SR models*

| Element | RW Model | CS Model | SR Model |
|---|---|---|---|
| Ag | 389.599 | 415.703 | **350.600** |
| Al | **251.753** | 269.512 | 261.026 |
| As | 15.597 | **15.272** | 22.461 |
| Au | 804.237 | 871.017 | **730.296** |
| Be | **18.698** | 18.708 | 22.356 |
| Bi | **577.023** | 579.292 | 642.437 |
| Ca | **51.090** | 51.179 | 54.630 |
| Cd | 223.538 | **221.784** | 348.205 |
| Co | 7116.245 | 7116.098 | **7065.640** |
| Cr | 430.023 | 399.499 | **377.888** |
| Cs | 309.743 | **301.347** | 319.562 |
| Cu | **775.554** | 798.968 | 791.484 |
| Fe | 14907.685 | 14834.926 | **14734.233** |
| Ge | 1193.508 | 1202.554 | **1172.808** |
| Hf | 128.947 | **128.803** | 142.706 |
| Hg | 449.682 | **443.437** | 526.792 |
| Ir | 57.778 | **57.503** | 90.183 |
| K | 282.080 | 208.341 | **194.546** |
| La | 36.960 | **36.433** | 40.842 |
| Mg | 132.690 | 145.240 | **124.597** |
| Mn | 105.495 | **105.270** | 142.826 |
| Mo | 1342.166 | **962.293** | 1077.956 |
| Na | 146.640 | 133.108 | **133.064** |
| Nb | **193.707** | 194.110 | 197.240 |
| Ni | 1293.893 | 1392.394 | **1225.163** |
| Pb | 229.296 | 240.192 | **186.585** |
| Pd | 119.394 | **111.726** | 286.532 |
| Pt | 619.980 | **611.384** | 616.560 |
| Rb | **56.401** | 58.036 | 130.098 |
| Re | 463.830 | 272.504 | **139.323** |
| Rh | **27.017** | 29.455 | 34.991 |
| Sb | 85.497 | **80.036** | 138.488 |
| Sc | 59.882 | 58.318 | **53.993** |
| Si | 718.435 | 732.982 | **688.499** |

| | | | |
|---|---|---|---|
| Sn | **784.704** | 823.040 | 803.525 |
| Ta | 3283.965 | **3211.131** | 3212.759 |
| Tl | **54.073** | 54.513 | 57.799 |
| V | 519.204 | **413.700** | 416.318 |
| W | 18891.667 | 13742.734 | **13332.490** |
| Y | 50.128 | 50.151 | **48.601** |
| Zn | 429.296 | 430.440 | **412.778** |